Stable isotope geochemistry of silicon in granitoid zircon

Martin Guitreau, Abdelmouhcine Gannoun, Zhengbin Deng, Marc Chaussidon, Frédéric Moynier, Bernard Barbarin, Johanna Marin-Carbonne

Stable isotope geochemistry of silicon in granitoid zircon

Martin Guitreau[1*], Abdelmouhcine Gannoun[1], Zhengbin Deng[2,3], Marc Chaussidon[2], Frédéric Moynier[2], Bernard Barbarin[1], and Johanna Marin-Carbonne[4]

[1] *Université Clermont Auvergne, CNRS, IRD, OPGC, Laboratoire Magmas et Volcans, UMR 6524, F-63000, Clermont-Ferrand, France.*

[2] *Université de Paris, Institut de Physique du globe de Paris, CNRS UMR 7154, F-75005 Paris, France*

[3] *Centre for Star and Planet Formation, Globe Institute, University of Copenhagen, Copenhagen, Denmark*

[4] *Institut des Sciences de la Terre, Université Lausanne, Géopolis Mouline, CH-1015 Lausanne, Switzerland*

[*] *Correspondence: martin.guitreau@uca.fr*

Keywords: Si isotopes, zircon, granite, LA-MC-ICP-MS

ABSTRACT

Zircon is often used to study granites (sensu lato) and continental crust because it is very resistant and can be analyzed for various isotope systems that provide time and source information about their parental melts. Granites with different petrological histories have distinct bulk-rock silicon isotope compositions but it is unclear if these differences are also detectable in zircon because of superimposed fractionation effects (e.g., related to temperature, silica content, magmatic processes). The present study explores the Si isotope signatures of zircon from various granite types to constrain their isotope fractionation behavior and uses

them as igneous petrogenetic tools, and possibly as granite source discriminators when zircon is found in detrital sediments. Our results show that although Si isotope compositions in zircon can be modified by secondary (post-crystallization) processes such as alteration/weathering and metamorphism, they are primarily controlled by zircon-melt isotope fractionation, which depends on both zircon crystallization temperature and magma silica content. Once these fractionation effects are understood and filtered out, a pattern emerges between Si isotope signatures of zircons from different granite types that is consistent with theoretical and experimental results as well as with known Si isotope differences at the bulk-rock scale. Silicon isotope ratios in zircon can track magma evolution (e.g., temperature and SiO_2 changes) and, hence, reveal complex processes that involved magma mingling, fractional crystallization, and/or multiple sources. This study, therefore, illustrates that Si isotopes in zircon can be used to investigate magma evolution and represents a useful complement to existing techniques in granite studies involving zircon (e.g., U-Th-Pb, Lu-Hf and O isotopes) provided that it is not used as a stand-alone technique.

1. Introduction

Silicon is a major component of silicates which make up most of the terrestrial mantle and crust. This chemical element has three stable isotopes 28, 29, and 30, with respective mean abundances of 92.23%, 4.68%, and 3.09% (Debievre and Taylor, 1993). Although developed long ago (e.g., Reynolds and Verhoogen, 1953; Clayton, 1978; Douthitt, 1982), Si isotope measurements have been applied to high-temperature geochemistry only recently (e.g., Shahar et al., 2009; Savage et al., 2011, Zambardi and Poitrasson, 2011) thanks to the advent of multicollection inductively coupled plasma

mass spectrometry (MC-ICP-MS; e.g., Georg et al., 2006) and optimized sample preparation procedure (i.e., alkali fusion) that allowed sufficiently high precision to observe natural variations. High-temperature Si isotope fractionation has consequently been studied in various contexts from cosmochemistry to igneous petrology allowing the establishment of bulk silicate Earth composition, which is distinct from most other planetary bodies (e.g., Georg et al., 2007; Savage et al., 2010; Shahar et al., 2011; Ziegler et al., 2012; Zambardi et al., 2013; Moynier et al., 2020), and the identification of a general igneous differentiation trend towards isotopically heavy Si isotope signatures for SiO_2-rich magmas (e.g., Savage et al., 2011; Poitrasson, 2017). In addition, it has been shown recently that granitoids - plutonic rocks formed by the slow cooling of a silica-rich magmas – exhibit distinct silicon isotope signatures depending on their chemical affinity and, hence, their source (e.g., Savage et al., 2012; André et al., 2019; Deng et al., 2019; Fig. 1). There are several ways to produce granitic magmas which is reflected in their chemical and isotopic compositions, ultimately responsible, together with pressure and temperature of crystallization, for the mineralogy of these plutonic rocks (e.g., Nédélec et al., 2015). Granites have been grouped into multiple types according to various classifications (e.g., peraluminous, metaluminous: Shand, 1943; A, I, S: Chappell and White, 1974; MPG, CPG, KCG, ACG, RTG, PAG: Barbarin, 1999; Table 1) essentially based on petrological and/or geochemical criteria. Granites, and more generally granitoids, are the major constituents of continents and it is, therefore, important to understand their formation and evolution over time because continents witnessed almost the entire Earth's evolutionary history.

Granites (sensu lato) most commonly contain zircon ($ZrSiO_4$) but in variable quantities depending on their origin and their degree of differentiation (e.g., Pupin, 1980; Samson et al., 2018). Zircon can be precisely and accurately dated using U-Th-

Pb isotope systems (e.g., Schoene, 2014) while the source of its parental magma can be approached using Hf and O isotopes (e.g., Patchett, 1983; Valley, 2003; Payne et al., 2016). Moreover, zircon is very resistant to weathering and erosion, and most elements diffuse very slowly within its lattice (e.g., Lee et al., 1997; Cherniak and Watson, 2003) making this mineral a very efficient time-capsule. Therefore, zircon has been a very useful source of information for granite petrogenesis. It is currently used in magmatic rocks and in detrital sediments, as an archive of the crust, to reconstruct the formation and evolution of continents (e.g., Roberts and Spencer, 2015 and references therein). Isotopic information provided by zircon should be interpreted differently for each granite type because of the distinct sources and petrogenetic processes involved in their formation (e.g., Barbarin, 1999; Bonin et al., 2019; Moyen, 2019). While only a few tools exist to determine the nature of the parental rock of a detrital zircon, they remain ambiguous and not always reliable (e.g., Belousova et al., 2006). Since granites of different types (A, I, S, and TTG) can have distinct Si isotope signatures (Savage et al., 2012; Poitrasson and Zambardi, 2015; André et al., 2019; Deng et al., 2019), it is likely that these differences can be retrieved from the Si isotope signature of zircon crystallized in these rocks.

The silicon stable isotope signature of an igneous rock can be controlled by that of its source, mineralogy, and melting/crystallization history (Savage et al., 2011; Poitrasson, 2017). In contrast, the Si isotope signature of a zircon is controlled by the degree of fractionation with its parental magma which essentially depends on the temperature of crystallization and the silica content (~degree of polymerization) of the surrounding melt that was studied theoretically and experimentally by Qin et al. (2016) and Trail et al. (2019). Co-precipitating phases (e.g., feldspar, quartz) can also play a role provided that they formed in equilibrium. However, post-crystallization processes

(e.g., radiation-damage, metamorphic recrystallization, alteration and weathering; Ewing et al., 2003; Vavra et al., 1999; Pidgeon et al., 2017, 2019) could possibly modify the Si isotope composition of a zircon. Trail et al. (2018) and Chowdhury et al. (2020) already presented Si isotope data for natural zircons and illustrated the potential of such application for very old igneous rocks. However, we thought it was appropriate to present a more extensive dataset of natural zircons from a wider variety of granite types to more deeply understand the fractionation behavior between zircon and its parental-rock and, hence, complement theoretical (Qin et al., 2016) and experimental (Trail et al., 2019) constraints. This, in turn, would provide a more robust reference frame for the interpretation of Si isotope data in zircon, and illustrate whether or not they can be used to discriminate granite types. Moreover, adding Si isotopes to the isotope tool-box currently applied to detrital zircons would help clarify the detrital record by better constraining the nature of zircon parental rocks and, therefore, prevent *ad hoc* interpretations of O and Hf isotope signatures.

In order to address these issues, this article presents Si isotope data obtained by laser-ablation multicollection inductively coupled plasma mass spectrometry (LA-MC-ICP-MS) and solution multicollection inductively coupled plasma mass spectrometry (S-MC-ICP-MS) for zircons from various granite types (4 A-type, 9 tonalite-trondhjemite-granodiorite: TTGs, 10 I-type, and 3 S-type; Tables 1 and S1), together with LA-ICP-MS trace element concentrations, U-Pb ages, and LA-MC-ICP-MS Lu-Hf isotope data for a subset of these zircons. We acknowledge that the A-I-S classification does not encompass the entire diversity of granites (e.g., Barbarin, 1996, 1999; Bonin et al., 2019; Moyen et al., 2016; Moyen, 2019) but have decided to use it in the present study because it has the advantage of being widely used. Our new results show that Si isotopes in zircon display a fractionation behavior that complies very well

with theory and experiment but, as suspected, secondary processes (e.g., weathering and metamorphism) can compromise the Si isotope signature of zircon. However, trace element signatures can help filter out altered compositions. Once fractionation behavior is understood and alteration filtered out, zircon Si isotope signatures are consistent with those in bulk-rocks.

2. Material and Methods

2.1. Samples

Zircon crystals studied here are from felsic igneous rocks of various affinities (e.g., A, I, S, TTG; Table 1) and correspond to separate minerals mounted in epoxy. The A-type granites analyzed in this study are from the Pikes Peak batholith, the Colorado Front Range (USA; Guitreau et al., 2016) and the Skjoldungen complex (Greenland; Nutman and Rosing, 1994) but we also analyzed a detrital zircon megacryst (1.5 cm long) from Tambani (Malawi) that derives from nepheline-bearing gneiss (Ashwal et al., 2007). Granites of I-type affinity analyzed here are from the Skellefte district (Sweden; Guitreau et al., 2014a and references therein), the Acasta Gneiss Complex (Canada; Guitreau et al., 2014b), and the French Massif Central (France; Barbarin, 1988a). Note that some of the Skellefte samples are not granites but sub-volcanic or porphyritic eruptive products that are chemically akin to and coeval with I-type granites with which they are associated. S-type granites are from the French Massif Central (Barbarin, 1988b) and correspond to cordierite granite (CPG) and two-mica granite (MPG; Barbarin, 1999). TTG studied here are from the Acasta Gneiss Complex (Canada), Barberton Greenstone Belt (South Africa), the Karelian craton (Finland), the Sharyzalgai uplift (Siberia), and the Napier Complex (East Antarctica). More

information about these samples can be found in Guitreau et al. (2012) and references therein.

2.2. Zircon imaging and analysis

2.2.1. Zircon CL and BSE imaging

Zircon cathodoluminescence (CL) and back-scattered electron (BSE) imaging was done at Laboratoire Magmas et Volcans (LMV, France) using a Jeol JSM-5910LV scanning electron microscope. Image acquisition was done using an acceleration voltage of 15 kV. Zircon imaging revealed internal textures which served as a tool to interpret zircon crystallization conditions (e.g., mafic or felsic igneous, metamorphic) as well as radiation damage accumulation and alteration effects (e.g., Corfu et al., 2003). This ultimately guided elemental and isotopic measurements that were located as much as possible in igneous domains (based on texture), except in the case of the zircon megacryst from Malawi in which domains corresponding to various crystallization conditions were purposely analyzed. Zircon crystals from TTGs and some I- and A-type granites were already imaged using CL/BSE technique and analyzed for Lu-Hf isotopes and U-Pb ages (Guitreau et al., 2012, 2014a, 2016, 2018, 2019).

2.2.2. Si isotope measurements by LA-MC-ICP-MS

Laser-ablation multicollection inductively coupled plasma mass spectrometry measurements were conducted at LMV using a Resonetics Resolution M-50E coupled to a Thermo Scientific Neptune Plus MC-ICP-MS, and followed closely the analytical protocol of Guitreau et al. (2020). Analytical conditions are provided in Table 2. Si isotopes were measured as traverses and the international zircon standard 91500 (from

a syenite; Wiedenbeck et al., 1995) was used as a bracketing standard. The zircon standards MudTank (from a carbonatite; Black and Gulson, 1978), KIM (from a kimberlite; Trail et al., 2018), AS3 (from a gabbro; Paces and Miller, 1993), Plešovice (hyperpotassic granulite; Sláma et al., 2008), and the synthetic standards MUN from the Memorial University of NewFoundland (Fisher et al., 2011) were used for quality check. Silicon isotope results are reported in Tables S2, S3, and 3 in delta notation, δ^{29}Si and δ^{30}Si, which express per mil deviations from a reference (quartz NBS 28), and are calculated using the following equations.

$$\delta^{X}Si = [(^{X}Si/^{28}Si_{sample})/ (^{X}Si/^{28}Si_{standard})-1] \times 1000$$

where X is either 29 or 30.

Throughout the manuscript, analytical uncertainty (i.e., within-run precision) is reported as 2 standard-errors (2SE) whereas external reproducibility (e.g. average of multiple analyses of the same zircon) is reported as 2 standard-deviations (2SD).

Silicon isotope data for AS3 zircon analyzed by LA-MC-ICP-MS in this study gave a δ^{30}Si of -0.47 ± 0.20‰ (2SD; Table 3), coherent with the value of -0.36 ± 0.35‰ (2SD obtained by Trail et al. (2018) using SIMS and the value of -0.44 ± 0.23‰ (2SD) obtained by Guitreau et al. (2020) using the same LA-MC-ICP-MS set-up as the present study. KIM zircon returned a LA-MC-ICP-MS δ^{30}Si of -0.41 ± 0.19‰ which is identical to the S-MC-ICP-MS value of -0.41 ± 0.01‰ (Trail et al. 2018) and the LA-MC-ICP-MS δ^{30}Si of -0.40 ± 0.23‰ from Guitreau et al. (2020). MudTank zircon analyzed in this study exhibit a LA-MC-ICP-MS δ^{30}Si of -0.38 ± 0.23‰ which is consistent, within error, with the S-MC-ICP-MS value of -0.34 ± 0.03‰ from Trail et al. (2018) and the δ^{30}Si of -0.47 ± 0.17‰ obtained by Guitreau et al. (2020). Plešovice zircon gave a δ^{30}Si of -0.44 ± 0.21‰ which is consistent with S-MC-ICP-MS data of -0.39 ± 0.06‰ from Guitreau et al. (2020). The synthetic MUN zircons analyzed in this

study exhibited δ^{30}Si of -1.61 ± 0.21‰ for MUN-0 and -2.02 ± 0.27‰ for MUN-1, which agree with values of -1.67 ± 0.14‰ and -2.08 ± 0.17‰, respectively, reported in Guitreau et al. (2020).

2.2.3. Si isotope measurements by S-MC-ICP-MS

We analyzed some of the zircons by S-MC-ICP-MS for the sake of comparison with LA-MC-ICP-MS measurements. Solution-MC-ICP-MS measurements were conducted during the same analytical sessions as zircon standard data from Guitreau et al. (2020) which used a technique modified after (Deng et al., 2019). Results for basalt reference material BHVO-2 normalized to quartz reference NBS28 analyzed using MC-ICP-MS alongside unknowns comply well with consensus values as we obtained δ^{29}Si and δ^{30}Si values of -0.14 ± 0.09‰ and -0.28 ± 0.15‰ (n = 60; 2SD) for BHVO-2 (δ^{30}Si = -0.29 ± 0.05‰; Schuessler and Von Blackenburg, 2014).

2.2.4. Trace element measurements in zircon

Trace element measurements were done at LMV by LA-ICP-MS using the same laser as for Si isotopes but coupled to a Thermo Scientific Element XR ICP-MS. Analytical spots were located on shallow lines formed by Si isotope analyses. Information regarding analytical conditions are given in Table 2. We used ^{28}Si as an internal standard and the synthetic glass standard SRM NIST 610 (Jochum et al., 2011) as a bracketing standard, whereas SRM NIST 612 (Jochum et al., 2011), 91500 (Wiedenbeck et al., 1995, 2004), MudTank (Gain et al., 2019), and AS3 (Takehara et al., 2018) zircon standards were analyzed for quality check. Batches of 6 unknowns and 3 quality-control standards were bracketed by 2 analyses of NIST 610. We used published Si concentration data when available but, otherwise, used stochiometric

values to convert ICP-MS counts/second into concentrations. Results are presented in Table S4. Elemental concentrations obtained for SRM NIST 612 were all consistent with published values within ≤ 7% (Jochum et al., 2011). Data for zircon standards analyzed in this study complied well with available published values for most elements (Table S4; Fig. S1). Note, however, that some elemental concentrations fall within the range of published values or close in the case of zircon reference materials that exhibit compositional differences between batches (MudTank and AS3) and/or because of alteration (e.g., Ca, Al, K, La contents).

2.2.5. U-Pb geochronology in Malawi zircon

The megacrystic zircon from Malawi was the only crystal studied for U-Pb and Lu-Hf in this work because its size allowed spatial resolution on various domains such as magmatic, metamorphic, and altered ones, and we wanted to investigate possible relationship between geochemical signatures within these domains. The regular size of normal zircons (~100-200 µm) does not allow these domains to be individualized. Therefore, this zircon was the appropriate candidate to test the effect of magmatic and metamorphic growth as well as secondary alteration on the geochemistry of zircon. In addition, a fair number of other zircons studied in this study were previously analyzed for U-Pb and Lu-Hf isotope systematics in earlier studies (Guitreau et al., 2012, 2014b, 2019). U-Th-Pb isotope measurements were done at LMV by LA-ICP-MS using the same instruments as for trace elements. Analytical spots were located next to lines formed during Si isotope analyses. Information regarding analytical conditions are given in Table 2. The zircon standard 91500 (1065.4 ± 0.3 Ma; Wiedenbeck et al., 1995) was used for bracketing whereas AS3 (1099.1 ± 0.5 Ma; Paces and Miller, 1993) and Plešovice (337.13 ± 0.37 Ma; Sláma et al., 2008) were analyzed as unknowns for

quality check. Data were acquired as batches of 6 unknowns bracketed by 4 measurements of 91500. Zircon U-Th-Pb data were processed using Glitter software (Van Achterbergh et al., 2001) and age calculations were done using a present-day $^{238}U/^{235}U$ of 137.818 (Hiess et al., 2012) and decay constants of $1.55125.10^{-10}$, $9.8485.10^{-10}$, and $4.9475.10^{-11}$ yr^{-1} for ^{238}U, ^{235}U and ^{232}Th, respectively (Jaffey et al., 1971; LeRoux and Glendenin, 1963). Concordia plots were built using the Isoplot software (Ludwig, 2008). Finally, semi-quantitative concentrations of U, Th, and Pb were determined by external normalization to 91500 as an additional means for interpreting U-Pb ages, notably to detect correlation between ages and U concentrations potentially arising from alteration facilitated by radiation-damage accumulation.

We obtained a Concordia age of 1097.5 ± 4.5 Ma (2SE; n = 7; MSWD = 0.52) and weighted average $^{206}Pb/^{238}U$ and $^{207}Pb/^{206}Pb$ ages of 1096.9 ± 6.6 Ma (2SE; n = 7; MSWD = 0.24), and 1097.3 ± 7.7 Ma (2SE; n = 7; MSWD = 0.24,) respectively, for AS3, and a Concordia age of 338.2 ± 2.9 Ma (2SE; n = 7; MSWD = 0.11), as well as 338.1 ± 2.9 Ma (2SE; n = 7; MSWD = 0.14) and 343 ± 22 Ma (2SE; n = 7; MSWD = 0.06), respectively, for Plešovice, which agree well with consensus ages (Wiedenbeck et al., 1995; Sláma et al., 2008). All results are available in Tables S5.

2.2.6. Lu-Hf isotope measurements in Malawi zircon

Lu-Hf isotope measurements were done at LMV by LA-MC-ICP-MS using the same instruments as for Si isotopes. Details regarding operating conditions can be found in Table 2. Measurements were done next to traces of U-Pb and Si isotope analyses. Zircons were analyzed as batches of 10 unknowns (4 standards and 6 samples) bracketed by REE-absent MUN zircon standard (MUN-0; Fisher et al., 2011). Standards analyzed as unknowns (91500, MudTank, and two MUN zircons with low

and high Yb/Hf ratios) were used to monitor data quality. Yb and Hf instrumental mass biases were determined using $^{173}Yb/^{171}Yb$ normalized to the value of 1.129197 (Vervoort et al., 2004) and $^{179}Hf/^{177}Hf$ normalized to 0.7325 (Stevenson and Patchett 1990). Lu fractionation was assumed to follow that of Yb (Fisher et al., 2014). Values of 0.793045 for $^{176}Yb/^{173}Yb$ (Vervoort et al., 2004) and 0.02655 for $^{176}Lu/^{175}Lu$ (Fisher et al., 2014) were used to correct isobaric interferences of ^{176}Yb and ^{176}Lu at mass 176. Since standards showed a slight shift, though reproducible, in $^{176}Hf/^{177}Hf$ after mass bias correction, we have used MUN-0 to determine an offset factor (i.e., difference between consensus and measured value) and correct all LA-MC-ICP-MS Lu-Hf analyses accordingly.

Malawi zircons were measured during two separate analytical sessions. The first session gave average $^{176}Hf/^{177}Hf$ measured in 91500 and MudTank of 0.282312 ± 0.000014 (2SD; n = 3) and 0.282508 ± 0.000023 (2SD; n = 2), respectively, and the second session gave 0.282315 ± 0.000057 (2SD; n = 4) for 91500 and 0.282511 ± 0.000023 (2SD; n = 4) for MudTank. These values compare well with consensus values of 0.282308 ± 0.000008 (Blichert-Toft, 2008) and 0.282507 ± 0.000006 (Woodhead and Hergt, 2005). The average $^{176}Hf/^{177}Hf$ measured during the first session in MUN_1-2b and MUN_4-2b were 0.282139 ± 0.000037 (2SD; n = 5), and 0.282131 ± 0.000034 (2SD; n = 5), respectively. The average $^{176}Hf/^{177}Hf$ measured during the second session in MUN_1-2b and MUN_3-2b were 0.282124 ± 0.000029 (2SD; n = 4), and 0.282127 ± 0.000034 (2SD; n = 4), respectively. Therefore, our results on MUN zircons are fully consistent with the value of 0.282135 ± 0.000007 reported in Fisher et al. (2011) which shows that our Lu-Hf data are accurately corrected for isobaric interferences created by ^{176}Yb and ^{176}Lu. We used the ^{176}Lu decay constant of $1.867.10^{-11}$ $yr^{-1}$from Scherer et al. (2001) and Söderlund et al. (2004) to calculate initial Hf isotopic compositions.

Uncertainties associated with the radiogenic-ingrowth correction were propagated using the algorithms of Ickert (2013) and ε_{Hf} values were calculated using CHUR values provided in Iizuka et al. (2015). Results can be found in Table S6.

3. Results

3.1. Si isotopes in zircon

Figure 1 presents all Si isotope data in the form of δ^{30}Si values for zircon crystals analyzed in this study by both laser-ablation MC-ICP-MS (colored squares; N = 188) and solution MC-ICP-MS (black dots; N = 5). It can be seen that zircon Si isotope compositions exhibit significant variations at essentially three different scales; (1) at the sample scale (within zircon population), (2) at the granite-type scale, and (3) between granite types. In fact, zircon populations have either reproducible (e.g., MZ2, 40-03, Klodden, LɣH; Fig. 1) or variable (e.g., Pikes Peak granite, AG09016, St-Julien, MARG; Fig. 1) δ^{30}Si values regardless of the type of granite considered. Similarly, not all samples of a particular granite-type exhibit the same average zircon δ^{30}Si values. Overall, zircon δ^{30}Si values are the highest in A-type granites (up to -0.13 ‰) and the lowest in S-type granites (down to -1.19 ‰), with an overall decrease forming the sequence A-type > TTG > I-type > S-type. However, there is too much overlap between the data to give confidence to this pattern as is.

Zircons from A-type granites have δ^{30}Si values that vary from -0.67 to -0.11‰ (average = -0.39‰; Fig. 1; Tables 3 and S3), which translate into apparent fractionation factors between zircon and whole-rock ($\Delta^{30}Si_{WR-Zrc} = \delta^{30}Si_{WR} - \delta^{30}Si_{zrc}$) of -0.04 to 0.52‰ (average = 0.24‰) when A-type bulk-rock δ^{30}Si of -0.15‰ is used (Savage et al., 2012). Zircons from TTGs have δ^{30}Si values that range from -0.83 to -0.29‰ (average = -0.50‰; Fig. 1; Tables 3 and S3), which translate into apparent fractionation

factors ($\Delta^{30}Si_{WR-Zrc}$) of 0.29 to 0.83‰ (average = 0.50‰) when TTG bulk-rock $\delta^{30}Si$ of 0.0‰ is used (Deng et al., 2019). Zircons from I-type granites have $\delta^{30}Si$ values that vary from -0.91 to -0.27‰ (average = -0.52‰; Fig. 1; Tables 3 and S3), which translate into apparent fractionation factors ($\Delta^{30}Si_{WR-Zrc}$) of 0.07 to 0.71‰ (average = 0.32‰) when I-type bulk-rock $\delta^{30}Si$ of -0.2‰ is used (Savage et al., 2012). Zircons from S-type granites have $\delta^{30}Si$ values that range from -1.19 to -0.47‰ (average = -0.77‰; Fig. 1; Tables 3 and S3), which translate into apparent fractionation factors ($\Delta^{30}Si_{WR-Zrc}$) of 0.17 to 0.89‰ (average = 0.46‰) when S-type bulk-rock $\delta^{30}Si$ of -0.3‰ is used (Savage et al., 2012). Si isotope data obtained in this study and calculated apparent fractionation factors are consistent with theoretical ($\Delta^{30}Si_{WR-Zrc}$ = 0.1 at 1300°C for an andesitic melt and 0.45‰ at 600°C for a rhyolitic melt; Qin et al., 2016) and experimental results ($\Delta^{30}Si_{WR-Zrc}$ = 0.32 to 0.56‰ at 700°C; Trail et al., 2019), as well as with available Si isotope data on minerals (zircon $\delta^{30}Si$ = -1.5 to 0.0‰; Trail et al., 2018).

3.2. Trace element concentrations

Results for trace elements are presented in Table S4 and Figures 2 and 3, which is organized according to 4 groups (A-type, TTG, I-type, and S-type), and in Figures S3 and S4, which presents the same data but for each sample separately. Trace element patterns in Figures 2 and S3 are normalized to chondrites (McDonough and Sun, 1995) and data for zircons from each granite type are reported with AS3 data for comparison. In contrast, Figures 3, S2 and S4 are normalized to AS3. Analyzed zircons exhibit trace element patterns that are consistent with that of AS3 (Fig. 2), though with two kinds of variations. The first one is "coupled variation" which means that all trace element contents vary coherently with each other, and this results in a vertical shift of the entire

pattern without changing its shape (Fig. 2). This is precisely the case for rare earth elements (REE) from Gd to Lu. The second kind is "decoupled variation" which corresponds to an increase in a chemical element content that is independent from the pattern. This increase is, however, often correlated between several elements such that when one element content increases the content of other elements increase too but to different extents. The best example corresponds to light REE (LREE) which show that when La content increases both Ce, Pr, Nd, and Sm increase but to a lesser extent as REE mass increases (Fig. 2). These two kinds of variations are visible in all groups but not in all zircon crystals. Decoupled variation describes the behavior of elements that are the most incompatible in zircon lattice (e.g., Al, Ca, Ga, Ba, LREE; Hoskin and Schaltegger, 2003; Pidgeon et al., 2019), whereas coupled variation corresponds to the behavior of least incompatible elements (e.g., Y, HREE, Hf, U). These two kinds of variations in trace element contents are shared by all granite types (Fig. 2). Zircon chemistry is very similar between all granite types which makes it difficult to use in granite-host identification as it was also acknowledged by Belousova et al. (2006). However, a few differences can be noted such as higher HREE content in S-type, an overall shallower REE pattern in A-type, and higher Nb and Ta contents in A-type zircons that create shoulders in the patterns visible in Figure 2. Zircon patterns reveal no or various extent of negative Eu and positive Ce anomalies, the latter being also blurred by an increase in La contents in some cases. Due to the size of the laser-beam and the scale of analyzed zircon crystals, variations in trace element contents and/or specific anomalies could not be associated with peculiar textural features, except in the Malawi zircon in which domains of different origins could be identified more readily (Figure 4). Figure 3 presents the same trace element data as in Figure 2 but normalized to AS3 which allows to more precisely observe the variation of chemical elements

around igneous values, represented by AS3, within each granite type as well as between granite types.

We determined Ti-in-zircon temperatures following the method of Ferry and Watson, (2007). Activities of SiO_2 ($aSiO_2$) and TiO_2 ($aTiO_2$) play a fundamental role in the validity of these temperature estimates which is why we used the software Rhyolite-MELTS (Gualda et al., 2012) to determine the appropriate activities at the zircon saturation temperature (T_{Zr}, Watson and Harrison, 1983; Miller et al., 2003; Boehnke et al., 2013), according to suggestions of Schiller and Finger (2019). We used T_{Zr} from both Watson and Harrison (1983) and Boehnke et al. (2013) calibrations as well as $T_{Zr/2}$ (i.e., T_{Zr} at half of the whole-rock Zr content; Schiller and Finger, 2019) but this only resulted in temperature variations within a narrow range of about 20°C. Similarly, changing the activity values within the main range of variation displayed in Schiller and Finger (2019) does not drastically change the temperature estimates. Furthermore, propagating all sources of uncertainty arising from the calibration curve for Ti-in-zircon temperature (Ferry and Watson, 2007), that of zircon saturation (Watson and Harrison, 1983; Boehnke et al., 2013), the input parameters and calculations behind the Rhyolite-MELTS model (Gualda et al., 2012), and the uncertainty on zircon Ti concentrations, we think that it seems unrealistic to expect a Ti-in-zircon temperature more precise than ~50°C. Consequently, we have finally used values of 0.95 for $aSiO_2$ and 0.45 $aTiO_2$, which are coherent conservative estimates of the true activities (Schiller and Finger, 2019), to determine zircon crystallization temperatures and have considered these values with a 50°C uncertainty. The Ti-in-zircon temperatures obtained for zircon standards MudTank and AS3 comply well with independent estimates from previous studies (Tables 3 and S4; Currie et al., 1992; Leu, 2016). Measured Ti-in-zircon temperatures gave 572-937°C for A-type granites (one

extreme at 1508°C), 716-974°C for TTGs (two extremes at 1107 and 1337°C), 758-970°C for I-type (two extremes at 1033 and 1312°C), and 776-1015°C for S-type granites (Table S4). These temperatures usually vary within a range of ≤ 100°C in each sample, except for S-type granites in which determined temperatures vary by up to ~250°C. Ti-in-zircon temperatures, therefore, vary from one sample to the other but without systematic difference between granite types. Temperature extremes mentioned above always have Ti concentrations that correlate with Al, and/or K, and/or Ca, which reach high values (e.g., 500-3000 ppm Al) that are inconsistent with elemental substitution during magmatic growth (Hoskin and Schaltegger, 2003; Bouvier et al., 2012). Some Ti-in-zircon temperatures are consistent with zircon-saturation temperatures (T_{zr}) whereas other disagree by more than 100°C (Table 3).

3.3. Malawi zircon

A back-scattered electron map of the megacrystic zircon (length = 1.5 cm) from Malawi reveals a very well-defined oscillatory zoning from core to rim (Figure 4), nevertheless, with visible concentric and radial fractures as well as metamorphic domains (dark grey zones) and biotite inclusions (black rounded areas). Various types of domains, labeled MZ1-MZ7, have been analyzed to track possible δ^{30}Si variations and link them to independent parameters such as crystallization (magmatic vs metamorphic) and alteration conditions, chemical composition, age, Hf isotope signature, and crystallization temperature. Traverses for Si isotope measurements by LA-MC-ICP-MS were done parallel to the magmatic zoning. Magmatic and metamorphic domains returned identical U-Pb dates (Table S5) which gave a Concordia age of 726.6 ± 2.3 Ma (2SE; MSWD = 0.92), identical to that of 730 Ma reported by Ashwal et al. (2007) for megacrystic zircons from nepheline-bearing gneisses from Malawi. Metamorphic

and magmatic domains display sharp differences in Th/U and U concentrations, which is also visible in $^{176}Lu/^{177}Hf$ ratios, but more importantly in $^{176}Hf/^{177}Hf$ and $\delta^{30}Si$ although differences are subtler in these isotopic systems (Figure 4). The chemical distinction between magmatic and metamorphic domains also translates into an overall downward shift of trace element patterns to lower concentrations in Figure 2, and in Ti-in-zircon temperatures change from 627-743°C for magmatic to 572-602°C for metamorphic domains (Table S4). The megacrystic zircon gave present-day $^{176}Hf/^{177}Hf$ from 0.282464 ± 0.000018 (2SE) to 0.282560 ± 0.000024 (2SE; Table S6) regardless of the domain analyzed, and $^{176}Lu/^{177}Hf$ from 0.0017 to 0.00004 with a sharp difference between magmatic and metamorphic domains, the latter having the smallest $^{176}Lu/^{177}Hf$ (Figure 4). Our new Lu-Hf isotope data are consistent with bulk-zircon solution data from Ashwal et al. (2007) that gave present-day $^{176}Hf/^{177}Hf$ of 0.282454 ± 0.000037 (2SE), 0.282466 ± 0.000057 (2SE), and 0.282475 ± 0.000057 (2SE) on three different zircon megacrysts for which the authors, however, did not measure $^{176}Lu/^{177}Hf$. $\delta^{30}Si$ for magmatic domains gave an average value of -0.43 ± 0.15‰ (2SD; average of individual analyses) identical to the S-MC-ICP-MS value of -0.46 ± 0.10‰ (2SD; Table 3), whereas metamorphic zones returned an average $\delta^{30}Si$ of -0.26 ± 0.19‰ (2SD; average of individual analyses). Note that $\delta^{30}Si$ are very reproducible within each magmatic domain and more variable in metamorphic domains (Figs 1 and 4). It should also be noted that slight variations in $\delta^{30}Si$ are visible between some of the magmatic domains. In fact, MZ2 has lower $\delta^{30}Si$ than MZ1, MZ3, and MZ4 but similar to MZ5 which is patchy-looking in BSE but does not have metamorphic signatures as in MZ6 and MZ7 (Figs. 2 and 4). Interestingly, magmatic domains have very variable $^{176}Lu/^{177}Hf$ ratios that are, however, reproducible within each zone (Fig. 4).

4. Discussion

As presented in the result section, Si isotope signatures in zircon can be either reproducible or variable within a zircon population, hence, at the sample scale (Fig. 1). Before interpreting zircon δ^{30}Si in terms of fractionation behavior between crystals and their parental melts (primary processes), we need to, first, evaluate the effects of secondary processes such as metamorphic recrystallization and alteration/weathering, which can be assessed using zircon internal texture and chemical composition.

4.1. Secondary causes of δ^{30}Si variations at the sample scale

The megacrystic zircon from Malawi (MZ; Fig. 4) presents good evidence for secondary modification of δ^{30}Si because metamorphic domains within this crystal display a distinct δ^{30}Si value (-0.26‰) compared to magmatic domains (-0.46‰). Metamorphic parts of MZ have typical characteristics of metamorphic zircons because they appear dark and homogeneous in BSE images (Fig. 4; Corfu et al., 2003), have very low Th/U (e.g., Vavra et al., 1999) and low Lu/Hf ratios, together with low trace element contents (Hoskin and Schaltegger, 2003). In addition, their estimated Ti-in-zircon temperature (~580°C) is lower than that of magmatic domains by about 100°C, and in itself low for a magmatic zircon. Given that the degree of fractionation between zircon and its parental melt/fluid increases as temperature decreases, the fact that metamorphic domains have higher δ^{30}Si than magmatic ones is good evidence for the formation of metamorphic zircon domains from high-δ^{30}Si medium, possibly crustal fluids (e.g., Kleine et al., 2018).

Metamorphism may also be responsible for the low δ^{30}Si of AG09-016 (TTG) zircons (Fig. 5A) which exhibit a well-defined positive correlation between Th/U ratios and δ^{30}Si values. Zircons from this 3947 Ma sample are known for having been affected

by metamorphism (e.g., Guitreau et al., 2018) but the ones analyzed for Si isotope were selected to be the most pristine according to CL and BSE images, as well as U-Th-Pb ages. This illustrates that metamorphism cannot always be straightforwardly detected in zircon and each isotope system has its own sensitivity to metamorphism. When considering the AG09-016 zircon that is least affected by metamorphism (i.e., with highest Th/U), its δ^{30}Si is very consistent with that of other TTG samples that have reproducible zircon δ^{30}Si (Figs 1 and 5A). Metamorphism appears to have opposite effects on δ^{30}Si values between MZ and AG09-016 zircons, which is likely controlled by local factors (e.g., nature of fluids, temperature, water-rock ratio in crustal fluids) as well as what actually happens during metamorphism (i.e., recrystallization or enhanced diffusion). The influence of metamorphism should therefore be evaluated on case-by-case basis.

Diffusion is a process known to possibly influence crystal elemental and isotope chemistry (e.g., Watson, 1996; Albarède, 2003; Cherniak and Watson, 2003) and we can, therefore, wonder if Si diffusion can play a role in the observed variability in zircon δ^{30}Si values (Fig. 1). Cherniak (2008) conducted diffusion experiments in zircon and concluded that Si diffuses in zircon lattice at rates similar to those for Ti, which are faster than those for U, Th, and Hf that are known to be essentially immobile in pristine zircon (e.g., Cherniak and Watson, 2003), but slower than those for O. For example, it would take 1.7 Ma for a silicon atom to diffuse over a radius of 1 µm at 650°C. The same distance would be reached after 12 Ga at 500°C. As a consequence, diffusion cannot account for Si isotope variations in studied zircon crystals.

Despite zircon being very resistant to most geological processes, radioactive element decay (e.g., U and Th) can significantly damage its lattice over time which can lead to metamictization of growth bands or domains (e.g., Holland and Gottfried, 1955;

Murakami et al., 1991) and formation of cracks (Lee and Tromp, 1995), altogether making zircon sensitive to secondary alteration (e.g., Corfu et al., 2003; Guitreau and Flahaut, 2019; Pidgeon et al., 2019). Since alteration and weathering can influence zircon chemical and isotopic compositions (e.g., Bouvier et al., 2012; Pidgeon et al., 2017, 2019; Guitreau and Flahaut, 2019) and that it has an effect on rocks and minerals (e.g., Ziegler et al., 2005; Opfergelt et al., 2012), we used trace element contents (i.e. non-formula elements) to assess zircon pristineness. The measured elevated contents of non-formula elements (e.g., Ca, K, Al) and their possible co-variation in some zircon crystals (Figs. 2 and S3; Table S4) testify that alteration/weathering occurred in some of the studied crystals (Pidgeon et al., 2019). However, most zircon populations displayed no relationship whatsoever between δ^{30}Si values and the concentration of alteration/weathering proxies. The 1.94 Ga (I-type) sample Knaften is one of the rare examples in which alteration/weathering seems to have potentially influenced the δ^{30}Si value of one zircon which is associated with a high Ca concentration (Fig. 5B). It is also evident in this sample that alteration/weathering is responsible for the high Ti concentration of the same zircon as illustrated by the positive correlation between Ca and Ti (Fig. 5C). This, in turn, means that the calculated Ti-in-zircon temperature for this crystal is over-estimated and no longer represents that of igneous crystallization. This testifies to the spurious nature of the extreme Ti-in-zircon temperatures mentioned in the result section as in all these cases Ti content correlates with that of light elements such as Al, Ca, K, (Table S4; Figs 2 and S3) which is diagnostic of external material input into zircon (e.g., Pidgeon et al., 2019).

As a consequence, alteration/weathering can affect zircon chemistry but does not always lead to modifications of zircon Si isotope signatures. However, this assertion should be regarded with some caution because Si isotopes were measured using

traverses, that covered a significant portion of each crystal, whereas trace element measurements were done using spots that were located unto the marks left by Si isotope analyses. Therefore, measurements were performed sequentially and on distinct material although spatially related. This is the major limitation of our approach and it is why the absence of significant influence of alteration/weathering on Si isotopes should not be considered as a firm conclusion. Nevertheless, our data still allow a fairly good understanding of the relationship between δ^{30}Si and trace elements since most of the analyzed zircons were pre-selected based on pristine-looking internal textures (fine oscillatory zoning) and existing chemical and/or isotopic data. It is, consequently, possible that a crystal was locally altered, which was detected by trace elements, although overall essentially pristine thereby giving non-altered Si isotope signatures that we can further discuss in an igneous context.

4.2. Primary causes of δ^{30}Si variations at the sample scale

Silicon isotope fractionation between zircon and its parental melt mostly depends on the temperature of zircon crystallization ($\Delta^{30}Si_{WR\text{-}Zrc} \propto 10^6/T^2$), and the degree of polymerization of SiO_4 in the melt (e.g., Grant, 1954; Poitrasson and Zambardi, 2015), which can be approached by the NBO/T parameter (Mysen et al., 1985) and SiO_2 content (e.g., Qin et al., 2016; Poitrasson, 2017; Trail et al., 2019). Ti-in-zircon temperature (Ferry and Watson, 2007) offers a good proxy for the crystallization temperature of zircon crystals and the vast majority of our samples have Ti-in-zircon temperatures that vary within ~100°C. According to experimental calibrations from Trail et al. (2019), δ^{30}Si variation only related to 100°C drop would go from 0.07‰ between 900° and 800°C to 0.14‰ between 700° and 600°C. This is in the case of zircon-quartz equilibration (SiO_2 concentration of ~100 wt%) for which the A value of

the fractionation equation (i.e., $\Delta^{30}Si_{Qz\text{-}Zrc} = A \times 10^6/T^2$) is 0.53 ± 014 (Trail et al., 2019). These fractionation values of 0.07 and 0.14‰ should, therefore, be regarded as maximum since the degree of fractionation between zircon and melt would be smaller for lower SiO_2 contents (Qin et al., 2016; Trail et al., 2019). These variations are smaller or equivalent to the analytical uncertainty of our analyses and would, hence, be undetected. Consequently, samples that display reproducible zircon $\delta^{30}Si$ associated with narrow Ti-in-zircon temperatures very likely formed from magmas with homogeneous SiO_2 contents (e.g., SKJ, 40-03, Klodden; Figs. 1 and 6) and homogeneous Si isotope compositions.

In contrast, samples with variable zircon $\delta^{30}Si$ can be due to crystallization over large temperature windows (>100°C) and/or from melts with variable SiO_2 contents either locally (e.g., mingling effects) or temporal (e.g., fractional crystallization effects). Figure 5D presents the only relationship between Ti-in-zircon temperatures and $\delta^{30}Si$ values visible in our dataset. It likely comes from the fact that this sample, MARG - a cordierite-bearing (S-type) granite – is the only sample that has a Ti-in-zircon temperature range of ~250°C (1015-775°C; Table S4). The relationship between $\delta^{30}Si$ values and temperature complies with theory and experiments but the degree of fractionation (0.72‰) is too large because a maximum $\delta^{30}Si$ variation of 0.16‰ should be expected if only temperature controlled the fractionation (Figs. 5D and 6D; Trail et al., 2019). In order to account for the excess fractionation, we can invoke a change in SiO_2 content of the parental melt but it does not entirely solve the problem (Figure 6D) because the degree of fractionation of these zircons, expressed as $\Delta^{30}Si_{WR\text{-}Zrc}$, exceed plausible values when a $\delta^{30}Si$ of -0.3‰ is assumed for S-type granites (Savage et al., 2011). A way to account for this strong evolution of MARG zircon $\delta^{30}Si$ is a source control because this granite is a crust-reworking product that involved clastic sediments

(e.g., Couturié, 1977), and low-temperature alteration of crustal rocks to form clay minerals result in the development of low δ^{30}Si signatures down to -2‰ (e.g., Ziegler et al., 2005; Opfergelt et al., 2012), opposite from what is seen with O isotopes (e.g., Valley, 2003; Bindeman, 2008). An additional consideration to account for the very large spread in δ^{30}Si and Ti-in-zircon temperature is to consider that some of the analyzed zircons, or some parts of these zircons, could be inherited since this is a common feature of crustally-derived granitoids (e.g., Villaros et al., 2012; Couzinié et al., 2021). This would, in turn, account for the very high temperature of 1015°C, which is hard to reconcile with the S-type nature of the Margeride granite.

The remaining samples with variable zircon δ^{30}Si have narrow Ti-in-zircon temperatures (e.g., Pikes Peak, Kristineberg; Figs. 1 and 6) which, therefore, cannot account for this within-zircon-population variability. The most likely explanation is local heterogeneities in SiO_2 concentrations and/or temperatures coming from magma mingling and/or mixing, or simply fractional crystallization. At 800°C, the difference between the δ^{30}Si of zircons formed from mafic (SiO_2 = 50 wt%) and felsic magmas (SiO_2 = 70 wt%) would be ~0.3‰ (Figure 6; Qin et al., 2016). These melts would most likely have distinct temperatures which would further increase the variability in δ^{30}Si values. One would have wished that zircon chemistry could help further support this hypothesis. However, trace element contents in zircon do not always significantly vary between crystals derived from mafic and felsic melts (e.g., Hoskin and Schaltegger, 2003), despite strong elemental variations between these two magma types. This, unfortunately, makes zircon a poor indicator of magma origin, except perhaps for A-type (Fig. S5), and account for the general absence of correlation between elemental concentrations and δ^{30}Si values. Interestingly, magma mingling has been reported for some of the samples exhibiting variations in zircon δ^{30}Si values. This is the case for

Kristineberg that belongs to the well-studied Jörn granitoid group for which Wilson et al. (1987) described multiple magma sources and interactions. Similarly, St-Julien-la-Vêtre granite is also known for obvious magma mingling between mafic and felsic end-members (Barbarin, 1988a).

A source control can also be invoked to account for some zircon δ^{30}Si variations, for example in S-type MARG (already discussed above), I-type Knaften and Kristineberg (Figure 6). In fact, Wasström (1993) described Knaften granitoids as subvolcanic plutons that intruded into mafic rocks and a supracrustal sequence containing greywacke, turbidite, and graphite-bearing argillites. If these supracrustals interacted with Knaften magmas, it would have lowered melt δ^{30}Si which could account for the sharp increase in Knaften $\Delta^{30}Si_{WR\text{-}Zrc}$ below 850°C that fall slightly above maximum fractionation (SiO_2 ~100 wt%; Fig. 6C) as calculated using a I-type bulk-rock δ^{30}Si value of -0.2‰. The typical A-type Pikes Peak granite involved both mantle-derived and crustally-derived, though not sedimentary, components (Smith et al., 1999; Guitreau et al., 2016) which likely resulted in magmas with variable SiO_2 contents, though with similar δ^{30}Si values. Silicon isotope composition of zircon, therefore, appears to be sensitive to complex magma evolution and track source changes and magma interactions.

Returning to the Malawi zircon example, magmatic domains MZ1, MZ3 and MZ4 have identical δ^{30}Si values, whereas MZ2, also magmatic, has a lower δ^{30}Si value (Figs. 1 and 4) despite MZ2 being located between growth bands MZ4 (innermost) and MZ3-MZ1 (outermost and being from the same growth bands but located in opposite parts of the zircon; Fig. 4). Our results also show that MZ2 crystallized at higher temperature than MZ3 and from a magma with apparently higher SiO_2 content (Table 3; Fig. 6). In addition, the central domain of the zircon (MZ5) that was analyzed but

interpreted as intermediate between magmatic and metamorphic because of patchy-looking internal texture (Figs. 1 and 4), has similar δ^{30}Si value as MZ2, and most of the trace element patterns, alongside Ti-in-zircon temperatures, are magmatic-looking (Fig. 2; Table 3). Therefore, MZ5 can be interpreted as the oldest magmatic growth zone of MZ and the coupled δ^{30}Si-temperature evolution from core (MZ5) to borders (MZ1-MZ3) reveal cycles of temperature increase and decrease associated with fluctuations in SiO_2 content over the course of zircon crystallization, possibly accounting for the large size of this crystal. These changes in magma composition, and/or crystallization temperature are consistent with the fact that ^{176}Lu/^{177}Hf ratio vary significantly between growth zones but this could also reveal equilibration with co-precipitating phases that changed during zircon growth.

4.3. Zircon δ^{30}Si variations within and between granite types

So far, our results combined with theoretical and experimental studies (Qin et al., 2016; Trail et al., 2019) allowed us to demonstrate that secondary processes, such as metamorphism and alteration/weathering, can modify zircon δ^{30}Si values, which could lead to an erroneous interpretation of the zircon parental melt composition, and that zircon-melt isotope fractionation is sensitive to crystallization temperature and magma silica content. Therefore, variations of zircon δ^{30}Si between samples of the same granite type as visible in Figure 1 can be accounted for by differences in zircon crystallization temperatures, whole-rock SiO_2 contents, and magma heterogeneities (i.e., Si elemental and isotopic compositions) linked to fractional crystallization and/or magma mingling and/or source controls as illustrated in Figure 6 and Table 3. This is for example the case between SKJ and Malawi magmatic domains because the former is higher temperature than the latter, though they have almost identical parental magma SiO_2

content (Fig. 6A; Table 3). Inversely, Pikes Peak granite has higher whole-rock SiO_2 content than SKJ, though similarly high temperatures (Fig. 6A). Klodden and Kristineberg belong to the same type of pluton (Jörn-type; Billström and Weihed, 1996) and have overlapping zircon $\delta^{30}Si$ values but they extend to lower values in Kristineberg (Figs 1 and 6C). This is well explained by the fact that Klodden has lower SiO_2 content than Kristineberg, in which zircon likely crystallized from evolving melts, hence, with changing SiO_2 content (Fig. 6C). Vargfors shows lower zircon crystallization temperatures and higher SiO_2 content than Klodden, which accounts for the differences in zircon $\delta^{30}Si$ (Table 3; Figs 1 and 6C). In contrast, differences visible between TTG zircon $\delta^{30}Si$ values are mostly due to metamorphic imprints because Steynsdorp (Stp) zircons exhibit similar relationship between $\delta^{30}Si$ values and Th/U ratios as AG09-016 zircons (Fig. 5A; Tables S3 and S4). Moreover, Napier zircons (78285007 and 78285013) are known for having been severely affected by metamorphism (e.g., Guitreau et al., 2019). It should also be noted that TTG samples studied in this contribution are the same, or equivalents from the same outcrops/plutons, as those analyzed for bulk-rock Si isotope compositions in Deng et al., (2019), except Napier samples 78285007 and 78285013, and they all gave a very consistent average bulk-rock $\delta^{30}Si$ value of -0.01 ± 0.02‰ (2 SD).

When all factors controlling zircon $\delta^{30}Si$ values are considered, one can understand why data from various granite types overlap in Figure 1. It is in fact because the range of zircon $\delta^{30}Si$ arising from fractionation related to melt composition (SiO_2 and $\delta^{30}Si$) and temperature variation could be larger than the difference between bulk-rock $\delta^{30}Si$ values. This is also close to the analytical precision and/or reproducibility of Si isotope measurements by LA-MC-ICP-MS and S-MC-ICP-MS (Table 3) which tends to increase natural variations. Yet, once all sources of variations are controlled

and secondary signatures corrected for, zircon δ^{30}Si values comply relatively well with bulk-rock δ^{30}Si pattern, as illustrated in Figure 7. This figure also reveals that the current analytical precision achieved by LA-MC-ICP-MS does not prevent this technique to be used but is a limiting factor that should be improved in the future.

A very good illustration of the misleading interpretation possibly arising from interpreting Si isotopes in zircon at face value is given by the two non-coeval Acasta samples AG09009 and AG09008g. The former and the latter belong to TTG (bulk-rock δ^{30}Si of 0.0‰; André et al., 2019; Deng et al., 2019) and I-type (bulk-rock δ^{30}Si of -0.2‰; Savage et al., 2012; Poitrasson and Zambardi, 2015), respectively, which is visible from both their bulk-rock chemical composition (Mojzsis et al., 2014) and their bulk-rock δ^{30}Si value (Deng et al., 2019). Despite these differences, they exhibit identical (and reproducible) zircon δ^{30}Si values of approximately -0.4‰ (Fig. 1; Table 3). This is well accounted for by the fact that AG09-009 has higher SiO_2 content than AG09-008g and its zircons have lower Ti-in-zircon (crystallization) temperatures than those from AG09-008g. These two factors together result in an increase of the isotope fractionation between zircons and their parental melt ($\Delta^{30}Si_{WR\text{-}Zrc}$) in AG09-009 compared to AG09-008g. Consequently, without knowledge of SiO_2 content and crystallization temperatures, it is virtually impossible to discriminate these Acasta samples from each other. In order for Si isotopes in zircon to be used effectively in out-of-context zircons (i.e., detrital crystals), a proxy for SiO_2 content or of the nature of the zircon parental melt should be used, as also pointed out in Qin et al. (2016) and Trail et al. (2019).

We took advantage of our dataset to calibrate the relationship between SiO_2 content and the A value, which was done indirectly by comparison with O isotopes in Qin et al. (2016) and using data from Trail et al. (2018) in Trail et al. (2019). Figure 8

presents the relationship between A value ($\Delta^{30}Si_{WR\text{-}Zrc}/10^6/T^2$) as a function of melt SiO_2 content that can be tentatively used to build more accurate figures such as those in Figure 6. We obtain the following relationship:

$$\Delta^{30}Si_{WR-Zrc} = \frac{10^6}{T^2} \times 0.00545x$$

With x being the whole-rock SiO_2 content in wt%, supposedly equivalent to that of the parental melt, and T the temperature in Kelvin (Fig. 8). Zircon crystallization temperature can be either obtained from Ti-in-zircon thermometer (Ferry and Watson, 2007) or possibly from zircon-saturation (Watson and Harrison, 1983; Miller et al., 2003). However, we observed in this study that Ti-in-zircon temperatures are quite consistent with zircon-saturation temperatures (Tzr; Table 3) in some cases (e.g., TTGs, MZ), uncertainty considered, but are quite different in others (e.g., SKJ, Klodden, Kristineberg). This mismatch is strongest in studied I-type granites, which illustrates the subjective character of T_{zr} that most likely come from the fact that granites do not often represent actual magmatic liquids. Therefore, Ti-in-zircon temperatures should be preferred because, contrary to T_{zr}, they can actually track zircon parental magma evolution.

5. Conclusions

This study focuses on the Si isotope composition of zircons from various granite types. We show that zircon $\delta^{30}Si$ can vary significantly at the sample scale (i.e., within a zircon population) but also between granites of the same type and between granite types. These variations are due to differences in zircon crystallization temperatures and parental magma SiO_2 contents, which makes zircon $\delta^{30}Si$ a good proxy for magma evolution. However, secondary processes, such as metamorphism and alteration/weathering, can affect zircon $\delta^{30}Si$ values but they can be readily identified on the basis of zircon

internal textures, as revealed by BSE/CL images, and trace-element geochemistry. Therefore, Si isotopes in zircon have promising applications to deciphering granitic magma evolution as well as granite-type discrimination that can be improved even further by reducing analytical uncertainty which is currently the major limitation of this technique.

Acknowledgements

We are grateful to Samuel B. Mukasa and Kjell Billström for providing Pikes Peak batholith and Skellefte samples, respectively. We are also grateful to Sam Broom-Fendley for providing the megacrystic Malawi zircon and to Dustin Trail for providing KIM and KL zircons as well as for stimulating discussions. Ken Koga and Fernando Corfu are thanked for help with Rhyolite-MELTS software and for sharing a fragment of 91500 zircon, resepctively. Jean-Luc Devidal is thanked for technical advice with trace element analysis by LA-ICP-MS. Martin Guitreau acknowledges financial support from the Région Auvergne through the Auvergne Fellowship program, LabEx ClerVolc (ANR-10-LABX-0006) and the French Agence Nationale de la Recherche through funded ANR-JC project *Zircontinents* (ANR-17-CE31-0021). This is Laboratory of Excellence ClerVolc contribution number 502. F.M. acknowledges funding from the European Research Council under the H2020 framework program/ERC grant agreement #637503 (Pristine). F.M. and M.C. thank the financial support of the UnivEarthS Labex programme at Université de Paris (ANR-10-LABX-0023 and ANR-11-IDEX-0005-02). Finally, we thank Jeffrey G Catalano and Helen M. Williams for handling our manuscript as well as Paul Savage and Franck Poitrasson for helpful and constructive reviews.

References

Albarède F. (2003) The thermal history of leaky chronometers above their closure temperature. *Geophy. Res. Lett.* **30**, 1015.

André L., Abraham K., Hofmann A., Monin L. Kleinhanns I. C. and Foley S. (2019). Early continental crust generated by reworking of basalts variably silicified by seawater. *Nat. Geosci.* **12**, 769-773.

Ashwal L. D, Armstrong R. A., Roberts R. J., Schmitz M. D., Corfu F., Hetherington C. J., Burke K. and Gerber M. (2007) Geochronology of zircon megacrysts from nepheline-bearing gneisses as constraints on tectonics setting: implications for resetting of the U-Pb and Lu-Hf isotopic systems. *Contrib. Mineral. Petrol.* **153**, 389-403.

Barbarin B. (1988a) Field evidence for successive mixing and mingling between the Piolard Diorite and the Saint-Julien-la-Vêtre Monzogranite (Nord-Forez, Massif Central, France) *Can. J. Earth Sci.* **25**, 49-59.

Barbarin B. (1996) Genesis of the two main types of peraluminous granitoids. *Geology* **24**, 205-298.

Barbarin B. (1999) A review of relationships between granitoid types, their origins and their geodynamic environments. *Lithos* **46**, 605-626.

Belousova E. A., Griffin, W. L. and O'Reilly S. Y. (2006) Zircon crystal morphology, trace element signatures and Hf isotopic composition as a tool for petrogenetic modelling: Examples from Eastern Australian granitoids. *J. Petrol.* **47**, 329-353.

Billström K. and Weihed P. (1996) Age and provenance of host rocks and ores in the Paleoproterozoic Skellefte district, northern Sweden. *Econom. Geol.* **91**, 1054-1072.

Bindeman I. (2008) Oxygen isotopes in mantle and crustal magmas as revealed by single crystal analysis. *Rev. Mineral. Geochem.* **69**, 445-478.

Black L. P. and Gulson B. L. (1978) The age of the Mud Tank Carbonatite, Strangways Range, Northern Territory. *J. Austral. Geol. Geophy.* **3**, 227-232.

Blichert-Toft J. (2008) The Hf isotopic composition of zircon reference material 91500. *Chem. Geol.* **253**, 252-257.

Boehnke P., Watson E. B., Trail D., Harrison T. M. and Schmitt A. K. (2013) Zircon saturation re-revisited. *Chem. Geol.* **351**, 324-334.

Bonin B., Janoušek V. and Moyen J.-F. (2019) Chemical variation, modal composition and classification of granitoids. *Geol. Soc. Spec. Pub.* **491**, 9-51.

Bouvier A.-S., Ushikubo T., Kita N. T., Cavosie A. J., Kozdon R. and Valley J. W. (2012) Li isotopes and trace elements as a petrogenetic tracer in zircon: insights from Archean TTGs and sanukitoids. *Contrib. Mineral. Petrol.* **163**, 745-768.

Chappell B. W. and White A. J. R. (1974) Two contrasting granite types. *Pac. Geol.* **8**, 173-174.

Cherniak D. J. and Watson E. B. (2003) Diffusion in zircon. In: Zircon. *Rev. Mineral. Geochem.* **53**, 113-143.

Cherniak D. J. (2008) Si diffusion in zircon. *Phys. Chem. Mineral.* **35**, 179-187.

Chowdhury W., Trail D., Guitreau M., Bell E., Buettner J. and Mojzsis S. J. (2020) Geochemical and textural investigations of the Eoarchean Ukaliq Supracrustals, Northern Québec (Canada). *Lithos* **372-373**, 105673.

Clayton R. N., Mayeda T. K. and Epstein S. (1978) Isotopic fractionation of silicon in Allende inclusions. *Proc. Ninth Lunar Planet. Sci. Conf.* **9**, 1267-1278.

Corfu F., Hanchar J. M., Hoskin P. W. O. and Kinny P. (2003) Atlas of zircon textures. In: Zircon. *Rev. Mineral. Geochem.* **53**, 469-500.

Couturié J.-P. (1977) Le massif granitique de la Margeride (Massif Central Français). PhD thesis Université Clermont II.

Couturié J.-P., Vachette M. and Vialette Y. (1979) Age namurien d'un laccolithe granitique différencié par gravité : le granite de la Margeride (M.C.F.). *C.R. Acad. Sci., Paris.* **289**, 449-452.

Couzinié S., Bouilhol P., Laurent O., Marko L. and Moyen J.-F. (2021) When zircon drowns: Elusive geochronological record of water-fluwed orthogneiss melting in the Velay dome (Massif Central, France). *Lithos* **384-285**, 105938.

Currie K. L., Knutson J. and Temby P. A. (1992) The Mud Tank carbonatite complex, central Australia - An example of metasomatism at mid-crustal levels. *Contrib. Mineral. Petrol.* **109**, 326-339.

Debievre P. and Taylor P. D. P. (1993) Table of the isotopic compositions of the elements. *Int. J. Mass Spectrom. Ion. Processes* **123**, 149-166.

Deng Z., Chaussidon M., Guitreau M., Puchtel I. S, Dauphas N. and Moynier F. (2019) An oceanic subduction origin for Archaean granitoids revealed by silicon isotopes. *Nat. Sci.* **12**, 774-778.

Didier J., Barbarin B., Gagny C., Leistel J. M., Kerrien Y. (1989) Notice explicative, Carte géol. France (l/50 000), feuille NOIRETABLE (695) - Orléans: Bureau de recherches géologiques et minières, 72 p. Carte géologique par Leistel J. M., Gagny C., Barbarin B., Jeambrun M., Pellaton N. C., Delfour J. (1988).

Douthitt C. B. (1982) The geochemistry of the stable isotopes of silicon. *Geochim. Cosmochim. Acta* **46**, 1449-1458.

Ewing R. C., Meldrum A., Wang L., Weber W. J. and Corrales L R. (2003) Radiation effects in zircon. In: Zircon. *Rev. Mineral. Geochem.* **53**, 427-467.

Ferry J. M. and Watson E. B. (2007) New thermodynamic models and revised calibrations for the Ti-in-zircon and Zr-in-rutile thermometers. *Contrib. Mineral. Petrol.* **154**, 429-437.

Fisher C.M., Hanchar J. M., Samson S. D., Dhuime B., Blichert-Toft J., Vervoort J. D. and Lam R. (2011) Synthetic zircon doped with hafnium and rare earth elements: A reference material for in situ hafnium isotope analysis. *Chem. Geol.* **286**, 32-47.

Fisher C.M., Vervoort J.D. and Hanchar, J.M. (2014) Guidelines for reporting zircon Hf isotopic data by LA-MC-ICP-MS and potential pitfalls in the interpretation of these data. *Chem. Geol.* **363**, 125–133.

Gain S. E. M., Gréau Y., Henry H., Belousova E., Dainis I., Griffin W. L. and O'Reilly S. Y. (2019) Mud Tank zircon: Long-term evaluation of a reference material for U-Pb dating, Hf isotope analysis and trace element analysis. *Geostand. Geoanal. Res.* **43**, 339-354.

Georg R. B., Reynolds B. C. Frank M. and Halliday A. N (2006) New sample preparation techniques for the determination of Si isotopic compositions using MC-ICP-MS. *Chem. Geol.* **235**, 95-104.

Georg R. B., Halliday A. N., Schauble E. A and Reynolds B. C. (2007) Silicon in the Earth's core. *Nature* **447**, 1102-1106.

Grant F.S. (1954) The geological significance of variations in the abundances of the isotopes of silicon in rocks. *Geochim. Cosmochim. Acta* **5**, 225-242.

Gualda G. A., Ghiorso M. S., Lemons R. V. and Carley T. L. (2012) Rhyolite-MELTS: a modified calibration of MELTS optimized for silica-rich, fluid-bearing magmatic systems. *J. Petrol.* **53**, 875-890.

Guitreau M., Blichert-Toft J., Martin H., Mojzsis S. J. and Albarède F. (2012) Hafnium

isotope evidence from Archean granitic rocks for deep-mantle origin of continental crust. *Earth Planet. Sci. Lett.* **337**, 211-223.

Guitreau M., Blichert-Toft J., Mojzsis S. J., Roth A. S. G., Bourdon B., Cates N. L. and Bleeker W. (2014a) Lu-Hf isotope systematics of the Hadean-Eoarchean Acasta Gneiss Complex (Northwestern Territories, Canada). *Geochim. Cosmochim. Acta* **135**, 251-269.

Guitreau M., Blichert-Toft J. and Billström (2014b) Hafnium isotope evidence for early-Proterozoic volcanic arc reworking in the Skellefte district (northern Sweden) and implications for the Svecofennian orogen. *Precamb. Res.* **252**, 39-52.

Guitreau M., Mukasa S. B., Blichert-Toft J. and Prado F. (2016) Pikes Peak batholith (Colorado, USA) revisited: A SIMS and LA-ICP-MS study of zircon U-Pb ages combined with solution Hf isotope composition. *Precamb. Res.* **280**, 179-194.

Guitreau M., Mora N. and Paquette J.-L. (2018) Crystallization and disturbance histories of single zircon crystals from Hadean-Eoarchean Acasta gneisses examined by LA-ICP-MS U-Pb traverses. *G-Cubed* **19**, 272-291.

Guitreau M. and Flahaut J. (2019) Record of low-temperature aqueous alteration of Martian zircon during the late Amazonian. *Nat. Comm.* **10**, 2457.

Guitreau M., Boyet M., Paquette J.-L., Gannoun A., Konc Z., Benbakkar M., Suchorski K. and Hénot M. (2019) Hadean protocrust reworking at the origin of the Napier Complex (Antarctica). *Geochem. Perspect. Lett.* **12**, 7-11.

Guitreau M., Gannoun A., Deng Z., Marin-Carbonne J., Chaussidon M. and Moynier F. (2020) Silicon isotope measurement in zircon by laser ablation multiple collector inductively coupled plasma mass spectrometry. *J. Anal. At. Spectrom.* **35**, 1597-1606.

Hiess J., Condon D. J., McLean N. and Noble S. R. (2012) $^{238}U/^{235}U$ systematics in terrestrial uranium-bearing minerals. *Science* **335**, 1610-1614.

Holland H. D. and Gottfried D. (1955) The effect of nuclear radiation on the structure of zircon. *Acta cryst.* **8**, 291-300.

Hoskin P. W. O. and Schaltegger U. (2003) The composition of zircon and igneous and metamorphic petrogenesis. In: Zircon. *Rev. Min. Geochem.* **53**, 27-62.

Ickert R. (2013) Algorithms for estimating uncertainties in initial radiogenic isotope ratios and model ages. *Chem. Geol.* **340**, 131–188.

Iizuka T., Yamaguchi T., Hibiya Y. and Amelin Y. (2015) Meteorite zircon constraints on the bulk Lu-Hf isotope composition and early differentiation of the Earth. *Proc. Nat. Acad. Sci.* **112**, 5331-5336.

Jaffey A. H., Flynn K. F., Glendenin L. E., Bentley W. C. and Essling A. M. (1971) Precision measurement of half-lives and specific activities of 235U and 238U. *Phys. Rev.* **C 4**, 1889.

Jochum K. P., Weis U., Stoll B., Kuzmin D., Yang Q., Raczek I., Jacob D. E., Stracke A., Birbaum K., Frick D. A., Günther D. and Enzweiler J. (2011) Determination of reference values for NIST SRM 610-617 glasses following ISO guidelines. *Geostand. Geoanal. Res.* **35**, 397-429.

Kleine B. I., Stefánsson A., Halldórsson S. A., Whitehouse M. J., Jónasson K**.** (2018) Silicon and oxygen isotopes unravel quartz formation processes in the Icelandic crust. *Geochem. Perspect. Lett.* **7**, 5-11.

Lee J.K.L. and Tromp J. (1995) Self-induced fracture generation in zircon. *J. Geophys. Lett.* **100**, 17753-17770.

Lee J. K. W, Williams I. S. and Ellis D. J. (1997) Pb, U, Th diffusion in natural zircon. *Nature* **390**, 159-162.

Le Roux L.J. and Glendenin L.E. (1963) Half-life of ^{232}Th. In: National Conference on Nuclear Energy, Application of Isotopes and Radiation. Proceedings of the National Conference on Nuclear Energy held in Pretoria, April 5–8 1963. South African Atomic Energy Board, Pelindaba, pp. 83–94.

Leu A. R. (2016) Geology and Petrology of the Wilder Lake Intrusion, Duluth Complex, Northeastern Minnesota. Thesis University of Minnesota.

Ludwig K.R. (2008) User's Manual for Isoplot 3.6, a Geochronological Toolkit for Microsoft Excel. *Berkeley Geochronology Center Special Publication* **4**.

McDonough W. F. and Sun S.-S. (1995) The composition of the Earth. *Chem. Geol.* **120**, 223-253.

Miller C. F., McDowell S. M. and Mapes R. W. (2003) Hot and cold granites? Implications of zircon saturation temperatures and preservation of inheritance. *Geology* **31**, 529-532.

Mojzsis S. J., Cates N. L., Caro G., Trail D., Abramov O., Guitreau M., Blichert-Toft J., Hopkins M. D. and Bleeker W. (2014) Component geochronology in the polyphase ca. 3920 Ma Acasta Gneiss. *Geochim. Cosmochim. Acta* **133**, 68-96.

Moyen J.-F., Laurent O., Chelle-Michou C., Couzinié S., Vanderhaeghe O., Zeh A., Villaros A. and Gardien V. (2016) Collision vs. Subduction-related magmatism: two contrasting ways of granite formation and implications for crustal growth. *Lithos* **277**, 154-177.

Moyen J.-F. (2019) Archean granitoids: classification, petrology, geochemistry and origin. In : Archean granitoids of India: Windows into Early Earth Tectonics (Dey and Moyen Eds.). Geol. Soc. Spec. Pub. **489**, 15-49.

Moynier F., Deng Z., Lanteri, A., Martins R., Chaussidon M., Savage P. and Siebert J. (2020) Metal-silicate silicon isotopic fractionation and the composition of the

bulk Earth. *Earth Planet. Sci. Lett.* **549**, 116468.

Murakami T., Chakoumakos B. C., Ewing R., Lumpkin G. R. and Weber W. J. (1991) Alpha-decay event damage in zircon. *Am. Min.* **76**, 1510-1532.

Nédélec A., Bouchez J.-L. and Bowden P. (2015) Granites: Petrology, structure, geological setting, and metallogeny. Oxford University Press, pp. 335.

Nutman A. P. and Rosing M. T. (1994) SHRIMP U-Pb zircon geochronology of the late Archaean Ruinnaesset syenite, Skjoldungen alkaline province, southeast Greenland. *Geochim. Cosmochim. Acta* **58**, 3515-3518.

Opfergelt S., Georg R. B., Delvaux B., Cabidoche Y.-M., Burton K. W and Halliday A. N (2012) Silicon isotopes and the tracing of desilication in volcanic soil weathering sequences, Guadeloupe. *Chem. Geol.* **326-327**, 113-122.

Paces J. B. and Miller J. D. Jr (1993) Precise U-Pb ages of Duluth complex and related mafic intrusion, Northeastern Minnesota: Geochronological insights to physical, petrogenetic, paleomagnetic, and tectonomagmaitc processes with the 1.1 Ga midcontinent rift system. *J. Geophy. Res.* **98**, 13997-14013.

Patchett P. J. (1983) Importance of the Lu-Hf isotopic system in studies of planetary chronology and chemical evolution. *Geochim. Cosmochim. Acta* **47**, 81-91.

Payne J. L., McInerney D. J., Barovich K. M., Kirkland C. L., Pearson N. J. and Hand (2016) Strengths and limitations of zircon Lu-Hf and O isotopes in modelling crustal growth. *Lithos* **248-251**, 175-192.

Pidgeon R. T., Nemchin A. A and Whitehouse M. J. (2017) The effect of weathering on U-Th-Pb and oxygen isotope system of ancient zircons from the Jack Hills, Western Australia. *Geochim. Cosmochim. Acta* **197**, 142-166.

Pidgeon R. T., Nemchin A. A., Roberts M. P., Whitehouse M. J. and Bellucci J. J. (2019) The accumulation of non-formula elements in zircons during

weathering: Ancient zircons from the Jack Hills, Western Australia. *Chem. Geol.* **530**, 119310.

Poitrasson F. and Zambardi T. (2015) An Earth-Moon silicon isotope model to teack silicic magma origins. *Geochim. Cosmochim. Acta* **167**, 301-312.

Poitrasson F. (2017) Silicon isotope geochemistry. *Rev. Mineral. Geochem.* **82**, 289-344.

Pupin J.-P. (1980) Zircon and granite petrology. *Contrib. Mineral. Petrol.* **73**, 207-220.

Qin T., Wu F., Wu Z. Q. and Huang F. (2016) First-principles calculations of equilibrium fractionation of O- and Si-isotopes in quartz, albote, anorthite and zircon. *Contrib. Mineral. Petrol.* **171**, 91.

Reynolds J. H. and Verhoogen J. (1953) Natural variations in the isotopic constitution of silicon. *Geochim. Cosmochim. Acta* **3**, 224-234.

Roberts N. W. and Spencer C. J. (2015) The zircon archive of continent formation through time. *Geol. Soc. Spec. Pub.* **389**, 211-223.

Rosing M. T., Nielsen T. F. D. and Vasudev V. N. (1988). An alkaline igneous province in the Skjoldungen area, South-East Greenland. *Geol. Surv. Greenland Int. Rep.* **145**, 55-66.

Samson S. D, Moecher D. P. and Satkoski A. M. (2018) Inherited, enriched, heated, or recycled? Examining potential causes of Earth's most zircon fertile magmatic episode. *Lithos* **314-315**, 350-359.

Savage P. S., Georg R. B., Armytage R. M. G., Williams H. M. and Halliday A. N. (2010) Silicon isotope homogeneity in the mantle. *Earth and Planet. Sci. Lett.* **295**, 139-146.

Savage P. S., Georg R. B., Williams H. M., Burton, K. W. and Halliday A. N. (2011) Silicon isotope fractionation during magmatic differentiation. *Geochim.*

Cosmochim. Acta **75**, 6124-6139.

Savage P. S., Georg R. B., Williams H. M., Turner S., Halliday A. N. and Chappell B. W. (2012) The silicon isotope composition of granites. *Geochim. Cosmochim. Acta* **92**, 184-202.

Scherer E., Münker C. and Mezger, K. (2001) Calibration of the lutetium–hafnium clock. *Science* **293**, 683–687.

Schiller D. and Finger F. (2019) Application of Ti-in-zircon thermometry to granite studies: problems and possible solutions. *Contrib. Mineral. Petrol.* **174**, 51.

Schoene B. (2014) U-Th-Pb geochronology. In: Holland H. and Turekian K. (Eds), *Treatise of geochemistry* (2nd ed., chap. 4.10, pp. 341-378). Oxford, UK: Elsevier.

Schuessler J. A. and von Blackenburg F. (2014) Testing the limits of micro-scale analyses of Si stable isotopes by femtosecond laser ablation multicollector inductively couple plasmla mass spectrometry with application to rock weathering. *Spectrochim. Acta Part B.* **98**, 1-18.

Shand S. J. (1943) Eruptive rocks. Their genesis, composition, classification, and their relations to ore-deposits. Wiley, New York, pp. 444.

Sláma J., Košler J., Condon D. J., Crowley J. L., Gerdes A., Hanchar J. M., Horstwood M. S. A., Morris G. A., Nasdala L., Norberg N., Schaltegger U., Schoene B., Tubrett M.N., Whitehouse M.J. (2008) Plešovice zircon – A new natural reference material for U–Pb and Hf isotopic microanalysis. *Chem. Geol.* **249**, 1-35.

Smith D. R., Noblett J., Wobus R. A., Unruh D. and Chamberlain K. R. (1999) A review of the Pikes Peak Batholith, Front Range, central Colorado: A “type example” of A-type granitic magmatism. *Rocky Mountain Geology* **34**, 289-312

Söderlund U., Patchett J.P., Vervoort J.D. and Isachsen C.E. (2004) The ^{176}Lu decay constant determined by Lu–Hf and U–Pb isotope systematics of Precambrian mafic intrusions. *Earth Planet. Sci. Lett.* **219**, 311–324.

Stevenson R.K. and Patchett, P.J. (1990) Implications for the evolution of continental crust from Hf isotope systematics of Archean detrital zircons. *Geochim. Cosmochim. Acta* **54**, 1683-1697.

Takehara M., Horie K., Hokada T. and Kiyokawa S. (2018) New insights into disturbance of U-Pb and trace-element systems on hydrothermally altered zircon via SHRIMP analyses of zircon form the Duluth gabbro. *Chem. Geol.* **484**, 168-178.

Talbert J.-C.and Duthou J.-L. (1983) Age carbonifère supérieur Rb/Sr du granite de Meymac (Massif Central français). *C.R. Acad. Sci., Paris* **296**, 1321-1323.

Trail D., Boehnke P., Savage P. S., Liu M.-C., Miller M. L. and Bindeman I. (2018) Origin and significance of Si and O isotope heterogenities in Phanerozoic, Archean, and Hadean zircon. *Proc. Nat. Acad. Sci.* **115**, 10287-10292.

Trail D., Savage P. S. and Moynier F. (2019) Experimentally determined Si isotope fractionation between zircon and quartz. *Geochim. Comsochim. Acta* **260**, 257-274.

Valley J. (2003) Oxygen isotopes in zircon. In: Zircon. *Rev. Mineral. Geochem.* 53, 343-385.

Van Achterbergh E., Ryan C. G., Jackson S.E. and Griffin W. L. (2001) Data reduction software for LA-ICP-MS: appendix. In: Sylvester P.J. (ed.) LaserAblation - ICP-Mass Spectrometry in the Earth Sciences: Principles and Applications. Mineralogical Association of Canada (MAC) Short Course Series **29**, 239–243.

Vavra G., Schmid R. and Gebauer D. (1999) Internal morphology, habit and U-Th-Pb microanalysis of amphibolite-to-granulite facies zircons: Geochronology of the Ivrea zone (Southern Alps). *Contrib. Mineral. Petrol.* **134**, 308-404.

Vervoort J. D., Patchett P. J., Söderlund U. and Baker M. (2004) Isotopic composition of Yb and the determination of Lu concentrations and Lu/Hf ratios by isotope dilution using MC-ICPMS. *G-Cubed* **5**, 1-15.

Villaros A., Buick I. S. and Stevens G. (2012) Isotopic variations in S-type granites: an inheritance from a heterogeneous source? *Contrib. Mineral. Petrol.* **163**, 243-257.

Wasström A. (1993) The Knaften granitoids of Västerbotten County, northern Sweden. In T. Lundqvist (ed.): Radiometric dating results. *Sveriges Geologiska Undersökning*, **Serie C823**, 60–64.

Watson E. B. and Harrison T. M. (1983) zircon saturation revisited: temperature and composition effects in a variety of crustal magma types. *Earth Planet. Sci. Lett.* **64**, 295-304.

Watson E. B. (1996) Dissolution, growth and survival of zircons during crustal fusion: kinetic principles, geological models and implications for isotopic inheritance. *Trans. Royal Soc. Edin. Earth Sci.* **87**, 43-56.

Wiedenbeck M., Allé P., Corfu F., Griffin W. L., Meier M., Oberli F., von Quadt A., Roddick J. C. and Spiegel W. (1995) Three natural zircon standards for U-Th-Pb, Lu-Hf, trace element and REE analyses. *Geost. Newslett.* **19**, 1-23.

Wiedenbeck M., Hanchar J. H., Peck W. H., Sylvester P., Valley J., Whitehouse M., Kronz A., Morishita Y., Nasdala L., Fiebig J., Franchi I., Girard J.-P., Greenwood R. C., Hinton R., Kita N., Mason P. R. D., Norman M., Ogasawara M., Piccoli P. M., Rhede D., Satoh H., Schulz-Dobrick B., Skår Ø., Spicuzza

M. J., Terada K., Tindle A., Togashi S., Vennemann T., Xie Q. and Zheng Y.-F. (2004) Further characterization of the 91500 zircon crystal. *Geostand. Geoanal. Res.* **28**, 9-39.

Wilson M. R., Sehlstedt S., Claesson L.-Å., Smellie J. A. T., Aftalion, M., Hamilton, J., and Fallick, A. E. (1987) Jörn: an early Proterozoic intrusive complex in a volcanic-arc environment, north Sweden. *Precamb. Res.* **36**, 201-225.

Woodhead J.D. and Hergt J.M. (2005) A preliminary appraisal of seven natural zircon reference materials for *in situ* Hf isotope determination. *Geostand. Geoanal. Res.* **29**, 183-195.

Zambardi T. and Poitrasson F. (2011) Precise silicon isotopes determination in silicate rock reference materials by MC-ICP-MS. *Geostand. Geoanal. Res.* **35**, 89-99.

Zambardi T., Poitrasson F., Corgne A., Méheut M., Quitte G. and Anand M. (2013) Silicon isotope variations in the inner solar system: Implications for the planetary formation, differentiation and composition. *Geochim. Cosmochim. Acta* **121**, 67-83.

Ziegler K., Chadwick O. A., White A. F., Brzezinski M. A. (2005) δ30Si systematics in a granitic saprolite, Puerto Rico. *Geology* **33**, 817–820.

Stable isotope geochemistry of silicon in granitoid zircon

Table 1. Sample details

Table 2. LA-ICP-MS and LA-MC-ICP-MS operating conditions

Table 3. Average Si isotope signatures of zircons analyzed in this study

Table 1

Granite type*		Origin	Name	Rock type	Age (Ma)	Reference
A-type	PAG	Tambani (Malawi)	MZ	Syenite (nepheline-bearing)	730	Ashwal et al., 2007
A-type	PAG	Skjoldungen (Greeland)	SKJ	Syenite	2690	Rosing et al., 1988; Nutman and Rosing, 1994
A-type	PAG	Pikes Peak batholith (USA)	YPP-20	Syenogranite	1066	Smith et al., 1999; Guitreau et al., 2016
A-type	PAG	Cripple Creek batholith (USA)	EMQ-5	Quartz-monzonite	1432	Guitreau et al., 2016
TTG	~ATG/ACG	Sharyzhalgai uplift (Siberia)	40-03	Trondhjemite	3400	Guitreau et al., 2012
TTG	~ATG/ACG	Acasta Gneiss Complex (Canada)	AG09009	Granodiorite	3600	Guitreau et al., 2012
TTG	~ATG/ACG	Karelian craton (Finlande)	H395	Trondhjemite	2800	Guitreau et al., 2012
TTG	~ATG/ACG	Barberton (South Africa)	NLS7.2	Trondhjemite	3245	Guitreau et al., 2012
TTG	~ATG/ACG	Sharyzalgai uplift (Siberia)	58-03	Tonalite	3392	Guitreau et al., 2012
TTG	~ATG/ACG	Barberton (South Africa)	Steynsdorp	Trondhjemite	3518	Guitreau et al., 2012
TTG	~ATG/ACG	Napier Complex (Antarctica)	78285007a	Tonalite	3794	Guitreau et al., 2012, 2019
TTG	~ATG/ACG	Napier Complex (Antarctica)	78285013	Granite	3857	Guitreau et al., 2012, 2019
TTG	~ATG/ACG	Acasta Gneiss Complex (Canada)	AG09016	Tonalite	3947	Guitreau et al., 2012
I-type	ATG	Acasta Gneiss Complex (Canada)	AG09008g	Tonalite	3975	Guitreau et al., 2012, 2014a, 2018; ; Mojzsis et al., 2014
I-type	ACG	Skellefte (Sweden)	Klodden	Granodiorite	1902	Guitreau et al., 2014b
I-type	KCG	Skellefte (Sweden)	Barsele	Dacite	1959	Guitreau et al., 2014b
I-type	ACG	Skellefte (Sweden)	Melestjärn	Quartz-felsdpar porphyritic flow	1889	Guitreau et al., 2014b
I-type	ACG	Skellefte (Sweden)	Kristineberg	Tonalite	1907	Guitreau et al., 2014b
I-type	KCG	St-Julien-la-vêtre, Forez (France)	St-Julien	Monzogranite	340	Didier et al., 1989
I-type	ACG	Skellefte (Sweden)	Vargfors	Ignimbite associated to granitoids	1875	Guitreau et al., 2014b
I-type	ATG	Acasta Gneiss Complex (Canada)	AG09017	Tonalite	3956	Guitreau et al., 2012, 2018; Mojzsis et al., 2014
I-type	ACG	Skellefte (Sweden)	Bjurvattnett	Sub-volcanic porphyritic rhyodacite	1884	Guitreau et al., 2014b
I-type	KCG	Skellefte (Sweden)	Knaften	Granodiorite	1940	Guitreau et al., 2014b
S-type	CPG	Margeride (France)	MARG	Monzogranite	323	Couturié et al., 1979
S-type	MPG	Hermitage, Forez (France)	LɣH	Monzogranite	325	Didier et al., 1989
S-type	CPG	Meymac (France)	Meymac	Monzogranite	295	Talbert and Duthou, 1983

* I-type = Infracrustal/Igneous, S-type = Supracrustal, A-type = Alkaline/Anorogenic, TTG = Tonalite, Trondhjemite, Granodiorite, PAG = Peralkaline and Alkaline Granitoids, ATG = Arc Tholeiitic Granitoids, ACG = Amphibole-bearing Calc-alkaline Granitoids, KCG = K-rich Calc-alkaline Granitoids, CPG = Cordierite-bearing Peraluminous Granitoids, MPG = Muscovite-bearing Peraluminous Granitoids)

Table 2

Analysis	***Si isotopes***			***Lu-Hf isotopes***								***U-Pb geochronology***	***Trace element concentrations***
Laboratory	Magmas et Volcans			*Magmas et Volcans*								*Magmas et Volcans*	*Magmas et Volcans*
Cup configuration	L3	C	H3	L4	L3	L2	L1	C	H1	H2	H3	N.A.	N.A.
Mass measured	28	29	30	171	173	174	175	176	177	178	179	204, 206, 207, 208, 232, 238	27-29, 39, 43, 44, 49, 51, 66, 71, 85, 88-91, 93, 96, 137, 139-141, 146, 147, 153, 157, 159, 163, 165, 166, 169, 172, 175, 178, 181, 206, 232, 238
ICP-MS model	Thermo Neptune *Plus*			Thermo Neptune *Plus*								Thermo Element XR	Thermo Element XR
Interface type	Jet (high sensitivity)			Jet (high sensitivity)								Jet (high sensitivity)	Jet (high sensitivity)
Cones	X-Cones			X-Cones								X-Cones	X-Cones
Resistors	10^{11} Ohms			10^{11} Ohms								Counting/Analog	Counting/Analog
Resolution	High (M/ΔM=7800)			Low								Low	Low
Forward Power	1200 W			1200 W								1300 W	1300 W
Auxiliary gas (Ar)	0.7-0.8 L/min			0.72 L/min								~0.7 L/min	0.75 L/min
Ar sample	~1 L/min			0.97 L/min								~1.0 L/min	1.01 L/min
Additional gas (N_2)	N.A.			4.0 mL/min								7.5 mL/min	6.5 mL/min
Oxide ThO/Th	N.A.			N.A.								~1%	~1%
SQUID	On			On								On	On
Data acquisition	*Time resolved analysis*			*Time resolved analysis*								*Time resolved analysis*	*Time resolved analysis*
Scanning mode	Static multi-collection			Static multi-collection								Peak-jumping	Mass scan
Integration time per isotope	1s			1s								5 ms	5 ms
Background counting time	20-30 s			20-30 s								20-30 s	20-30 s
Sample measurement time	40-60s			50s								60 s	60 s
Measurement type	Standard bracketing			Internal and external normalization								Standard bracketing	Standard bracketing
External standard	91500, KIM, AS3, Plešovice, MudTank, MUN zircons			91500, Mud Tank, MUN zircons								91500, AS3, Plešovice	NIST 610, NIST 612, 91500, MudTank, AS3
Laser model	*Resonetics Resolution M-50E*			*Resonetics Resolution M-50E*								*Resonetics Resolution M-50E*	*Resonetics Resolution M-50E*

Wavelength	193 nm	193 nm	193 nm	193 nm
Pulse duration	5 ns	5 ns	5 ns	5 ns
Energy	2-5 mJ	~3.2 mJ	~3.5 mJ	~3.5 mJ
Fluence	~3 J/cm2	~3.6 J/cm2	~2.5 J/cm2	~2.5 J/cm2
Frequency	6 Hz	6 Hz	4 Hz	2 Hz
Spot size	33 µm	40 µm	33 µm	33 µm
Carrier gas	He	He	He	He
Carrier gas flow	0.65-0.75 L/min	0.7 L/min	0.65 L/min	0.75 L/min
Traverse rate	1.6 µm/s	N.A.	N.A.	N.A.

Table 3

			Relative to NBS 28											
MC-ICP-MS method	**Granite type**	**Name**	**δ29Si (‰)**	**2SD**	**δ30Si (‰)**	**2SD**	**n**	**$\Delta^{30}Si_{WR-zrc}$ (‰)**	**WR SiO_2**	**TZr**	**TZr***	**Zircon T (°C)**	**$10^6/T^2$**	**A**
Laser ablation	A-type	MZ1	-0.25	0.11	-0.38	0.13	6	0.23	58.10	560	626	-	-	-
Laser ablation	A-type	MZ2	-0.24	0.10	-0.54	0.05	6	0.39	58.10	560	626	699	1.06	0.37
Laser ablation	A-type	MZ3	-0.21	0.11	-0.41	0.08	6	0.26	58.10	560	626	649	1.18	0.22
Laser ablation	A-type	MZ4	-0.24	0.06	-0.40	0.12	6	0.25	58.10	560	626	-	-	-
Laser ablation	A-type	MZ5	-0.25	0.07	-0.50	0.05	6	0.35	58.10	560	626	657	1.16	0.30
Laser ablation	A-type	MZ6	-0.17	0.10	-0.29	0.22	6	0.14	58.10	-	-	-	-	-
Laser ablation	A-type	MZ7	-0.14	0.08	-0.24	0.17	6	0.09	58.10	-	-	580	1.37	0.06
Laser ablation	A-type	SKJ	-0.16	0.14	-0.22	0.11	6	0.07	57.73	630	695	828	0.82	0.08
Laser ablation	A-type	Pikes Peak	-0.22	0.11	-0.43	0.27	6	0.28	68.07	874	895	911	0.71	0.39
Laser ablation	A-type	EMQ-5	-0.31	0.05	-0.55	0.18	6	0.40	60.98	834	862	-	-	-
Laser ablation	TTG	40-03	-0.18	0.09	-0.37	0.10	5	0.37	71.31	716	756	758	0.94	0.39
Laser ablation	TTG	AG09009	-0.23	0.09	-0.40	0.13	5	0.40	71.62	828	852	799	0.87	0.46
Laser ablation	TTG	H395	-0.27	0.12	-0.43	0.16	5	0.43	68.80	810	836	-	-	-
Laser ablation	TTG	NLS7.2-08	-0.17	0.12	-0.39	0.18	5	0.39	66.68	738	778	-	-	-
Laser ablation	TTG	58-03	-0.25	0.16	-0.46	0.15	5	0.46	69.43	764	802	-	-	-
Laser ablation	TTG	Stp	-0.29	0.10	-0.57	0.14	5	0.57	73.91	771	805	854	0.79	0.72
Laser ablation	TTG	78285007a	-0.36	0.11	-0.60	0.20	5	0.60	66.90	640	695	-	-	-
Laser ablation	TTG	78285007na	-0.28	0.19	-0.55	0.17	6	0.55	66.90	640	695	-	-	-
Laser ablation	TTG	78285013	-0.37	0.10	-0.57	0.17	7	0.57	71.88	602	661	1157	0.49	1.18
Laser ablation	TTG	AG09016	-0.27	0.14	-0.59	0.27	7	0.59	66.23	918	925	933	0.69	0.86
Laser ablation	I-type	AG09008g_8	-0.22	0.12	-0.42	0.10	7	0.22	56.71	790	835	-	-	-
Laser ablation	I-type	Klodden	-0.23	0.07	-0.40	0.10	6	0.20	57.75	641	692	888	0.74	0.27
Laser ablation	I-type	Barsele	-0.17	0.12	-0.35	0.25	5	0.15	68.10	824	838	-	-	-
Laser ablation	I-type	Melestjärn	-0.28	0.16	-0.46	0.42	5	0.26	75.03	767	798	-	-	-
Laser ablation	I-type	Kristineberg	-0.29	0.12	-0.49	0.26	5	0.29	62.10	725	769	933	0.69	0.42

Laser ablation	I-type	St-Julien	-0.33	0.25	-0.62	0.30	5		0.42	64.80	-	-	-	-	-
Laser ablation	I-type	Vargfors	-0.28	0.10	-0.53	0.17	6		0.33	71.97	737	776	823	0.83	0.40
Laser ablation	I-type	AG09017	-0.31	0.14	-0.61	0.21	7		0.41	60.16	774	808	-	-	-
Laser ablation	I-type	Bjurvattnett	-0.35	0.11	-0.65	0.18	6		0.45	69.35	770	798	-	-	-
Laser ablation	I-type	Knaften	-0.31	0.23	-0.69	0.33	6		0.49	74.60	710	753	907	0.72	0.68
Laser ablation	S-type	MARG	-0.45	0.29	-0.80	0.59	4		0.50	68.23	-	-	906	0.72	0.70
Laser ablation	S-type	LYH	-0.38	0.12	-0.74	0.11	5		0.44	74.20	-	-	-	-	-
Laser ablation	S-type	Meymac	-0.41	0.08	-0.75	0.18	6		0.45	70.38	-	-	831	0.82	0.55
Solution	TTG	40-03-Zrc	-0.21	0.09	-0.42	0.13	4		0.42	71.31	716	756	758	0.94	0.45
Solution	TTG	H395-Zrc	-0.19	0.03	-0.41	0.07	4		0.41	68.80	810	836	-	-	-
Solution	I-type	Kristineberg-Zrc	-0.21	0.07	-0.42	0.10	6		0.22	62.10	725	769	933	0.69	0.32
Solution	A-type	EMQ-5-Zrc	-0.22	0.03	-0.40	0.08	3		0.25	60.98	834	862	-	-	-
Solution	A-type	MZ-2	-0.20	0.02	-0.46	0.10	4		0.31	58.10	560	626	699	1.06	0.29
Laser ablation	Standard	AS3	-0.25	0.14	-0.47	0.20	16		0.18	50.00	-	-	970	0.65	0.27
Laser ablation	Standard	KIM	-0.21	0.13	-0.41	0.19	12		0.12	35.00	-	-	678	1.11	0.11
Laser ablation	Standard	MudTank	-0.19	0.11	-0.38	0.23	5		0.09	15.00	-	-	789	0.89	0.10
Laser ablation	Standard	Plešovice	-0.23	0.08	-0.44	0.21	5		0.24	61.00	-	-	-	-	-
Laser ablation	Standard	MUN-0	-0.84	0.14	-1.61	0.21	14	-		-	-	-	-	-	-
Laser ablation	Standard	MUN-1	-1.04	0.15	-2.02	0.27	16	-		-	-	-	-	-	-

$\Delta^{30}Si_{WR\text{-}zrc}$ is calculated using $\delta^{30}Si_{WR}$ of -0.15‰ for A-type, 0.0‰ for TTG, -0.2‰ for I-type, -0.3‰ for S-type, and -0.29‰ for AS3, KIM and MudTank.

Tzr calculated using the calibration of Boehnke et al. (2013) whereas Tzr was calculated using the original calibration of Watson and Harrison (1983)*

Zircon T°C is the average Ti-in-zircon temperature determined for each sample

Temperature is expressed in Kelvin in $10^6/T^2$

A is the constant in the fractionation law: $\Delta^{30}Si_{WR\text{-}zrc} = A*10^6/T^2$

Stable isotope geochemistry of silicon in granitoid zircon

Figures

Figure 1. Si isotope results for zircon crystals analyzed in this study by S-MC-ICP-MS (black spots) and LA-MC-ICP-MS (colored squares) in the form of δ^{30}Si values. Also indicated are the average δ^{30}Si for mantle zircon (-0.38 ± 0.04 ‰; 2SD; Trail et al., 2018) together with bulk-rock average δ^{30}Si values for major granite types (A-, I-, S- and TTGs; Savage et al., 2012; Poitrasson and Zambardi et al., 2015; Deng et al., 2019).

Figure 2. Chondrite-normalized (McDonough and Sun, 1995) multi-element plots for granitic zircons. Color-coding is the same as in Figure 1. Data for AS3 zircon are from this study and given for comparison.

Figure 3. Zircon reference AS3-normalized multi-element plots for granitic zircons. Color-coding is the same as in Figure 1. Data for AS3 zircon are from this study (Table S4) and given for comparison. The AS3 elemental values used to normalize zircon data are averages of measurements from this study for which Al concentration was below 1 ppm in order to obtain a least altered and representative igneous composition.

Figure 4. Back-scattered electron (BSE) image of the megacrystic zircon from Malawi with details about *in-situ* measurement locations (MZ1-MZ7). Also indicated are isotopic and chemical information obtained from these zones. Note the general fine oscillatory zoning from core to rim typical of magmatic zircons on which is superimposed dark and homogeneous metamorphic zones together with fractures and mid-grey patchy domains. Red symbols in Figures B-G correspond to analyses done within magmatic domains visible in Figure A, whereas grey symbols are from metamorphic domains and blue symbols from "intermediate" patchy domains. See text for details.

Figure 5. Composite figure that presents zircon δ^{30}Si and chemical data from TTGs (A), from I-type granite (B) and (C), and from S-type granite (D). Figure (A) shows that metamorphism, which is marked by a decrease of Th/U down to < 0.2, lowers zircon δ^{30}Si. Note that AG09-016 zircons with the highest δ^{30}Si value, which also have typical igneous Th/U, fall in the range of δ^{30}Si values exhibited by "pristine" zircons from other TTGs. Figure (B) shows that high Ca concentration in zircon, which is a sign of alteration/weathering, can possibly drag δ^{30}Si down. Ti concentration in the same altered zircon has consequently been increased (Figure C), hence, compromising the meaningfulness of determined Ti-in-zircon temperature. Finally, Figure D presents the only relationship we obtained in our dataset between δ^{30}Si and Ti-in-zircon temperature. As illustrated by the arrows, this relationship cannot solely be explained by temperature decrease but has to involve a change in SiO_2, and perhaps a source control.

Figure 6. Silicon isotope fractionation between zircon and melt, expressed as $\Delta^{30}Si_{WR-Zrc}$, as a function of Ti-in-zircon temperature (T°C) and $10^6/T^2$ (in Kelvin). We only plotted samples for which we analyzed trace elements and that were not affected by secondary processes (see text fo details). Also indicated are SiO_2 contents of corresponding whole-rock (WR) samples (Table 3). The solid and dashed lines with associated SiO_2 contents are from Trail et al. (2019). $\Delta^{30}Si_{WR-Zrc}$ were calculated assuming bulk-rock A-type granite $\delta^{30}Si$ of -0.15‰, TTG $\delta^{30}Si$ of -0.0‰, I-type $\delta^{30}Si$ of -0.20‰, and S-type granite $\delta^{30}Si$ of -0.30‰ (Deng et al., 2019). Note the general good consistency between zircon group positions and WR SiO_2 contents for samples with simple distribution (e.g., SKJ = 58 wt% SiO_2; Klodden = 58 wt% SiO_2; 40-03 = 71 wt% SiO_2; AG09-009 = 72 wt% SiO_2; Meymac = 70 wt% SiO_2). Also note the spread in $\Delta^{30}Si_{WR-Zrc}$ values for other samples (e.g., Pikes Peak granite, Knaftern, MARG) that indicate heterogeneous SiO_2 that most likely arise from fractional crystallization, magma mingling, and/or change in the source of parental magma, or crustal assimilation. In fact, clay-rich sediments can have $\delta^{30}Si$ down to approximately -2‰, thereby artificially increasing the $\Delta^{30}Si_{WR-Zrc}$ (Ziegler et al., 2005; Opfergelt et al., 2012; Trail et al., 2018). Color-coding is the same as in Figure 1.

Figure 7. Silicon isotope signatures of analyzed zircons filtered for secondary processes and grouped according to major granite types. Color-coding is the same as in Figure 1. Each circle corresponds to the average zircon $\delta^{30}Si$ obtained from one sample. Also indicated are the values for the various granite types (Savage et al., 2012; Poitrasson and Zambardi, 2015; Deng et al., 2019) and the within-run precision of LA-MC-ICP-MS analyses. Note the similar pattern between zircon and whole-rock $\delta^{30}Si$.

Figure 8. Binary plot showing the relationship between A value and whole-rock SiO_2 content (A) and its consequence for the $\Delta^{30}Si_{WR\text{-}Zrc}$ versus WR SiO_2 plot (B) used for interpretations of zircon $\delta^{30}Si$ and Ti-in-zircon temperature. Color-coding in (A) is the same as in Figure 1. Numbers next to lines are respective A values in (B). Also reported in (B) are the slopes and corresponding SiO_2 contents from Qin et al. (2016) and Trail et al. (2019). Compared to this study, slopes (i.e., A values) derived from theory (Qin et al., 2016) seem to under-estimate Si isotope fractionation between zircon and high-SiO_2 melts, whereas slopes from experiments tend to under-estimate Si isotope fractionation between zircon and low-SiO_2 melts (Trail et al., 2019). However, note that uncertainties on A values are similar to those on $\delta^{30}Si$, and hence on $\Delta^{30}Si_{WR\text{-}Zrc}$, that vary between 0.1 and 0.2 (2SD absolute values) which is not shown in (B). Moreover, the fit in (A) is linear but the actual relationship between A value and SiO_2 may not be linear as noted in Trail et al. (2019) and could instead require a polynomial fit such as the modeling of fractionation behavior done in Qin et al., (2016).

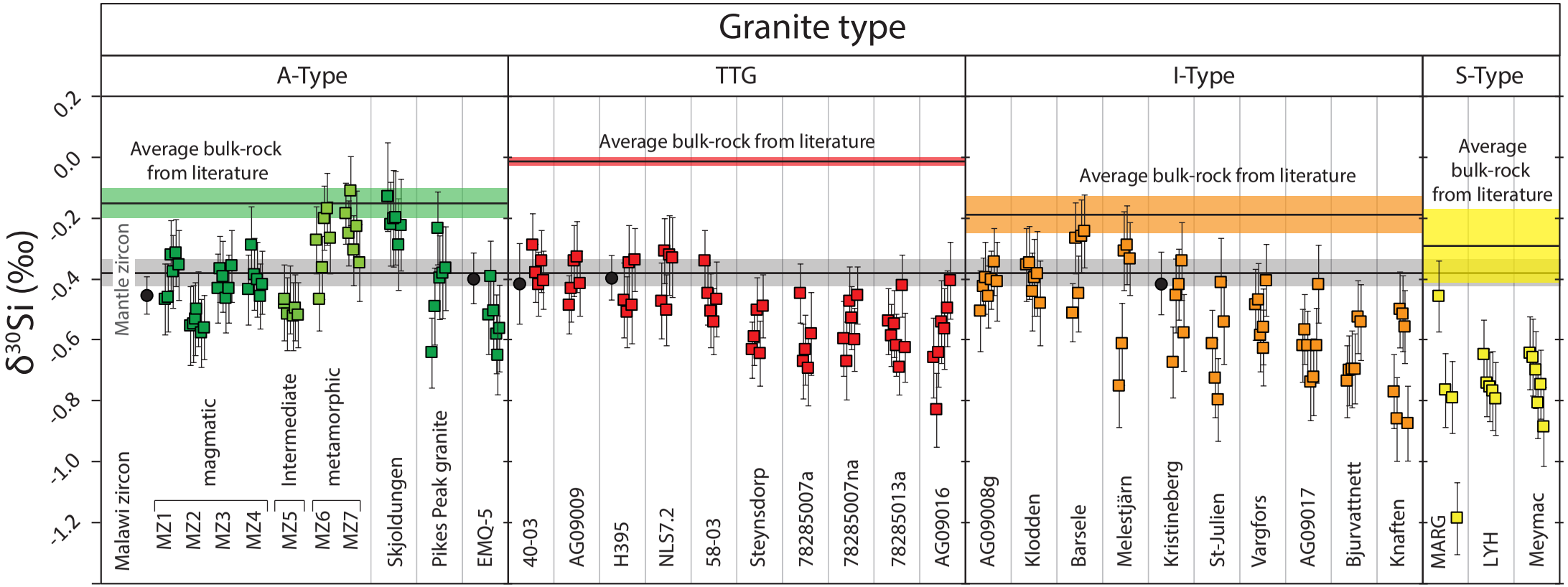
Granite type
A-Type
TTG
I-Type
S-Type
δ30Si (‰)
0.2
0.0
-0.2
-0.4
-0.6
-0.8
-1.0
-1.2
Average bulk-rock from literature
Average bulk-rock from literature
Average bulk-rock from literature
Average bulk-rock from literature
Mantle zircon
Malawi zircon
MZ1
MZ2
MZ3
MZ4
magmatic
MZ5
Intermediate
MZ6
MZ7
metamorphic
Skjoldungen
Pikes Peak granite
EMQ-5
40-03
AG09009
H395
NLS7.2
58-03
Steynsdorp
78285007a
78285007na
78285013a
AG09016
AG09008g
Klodden
Barsele
Melestjärn
Kristineberg
St-Julien
Vargfors
AG09017
Bjurvattnett
Knaften
MARG
LYH
Meymac

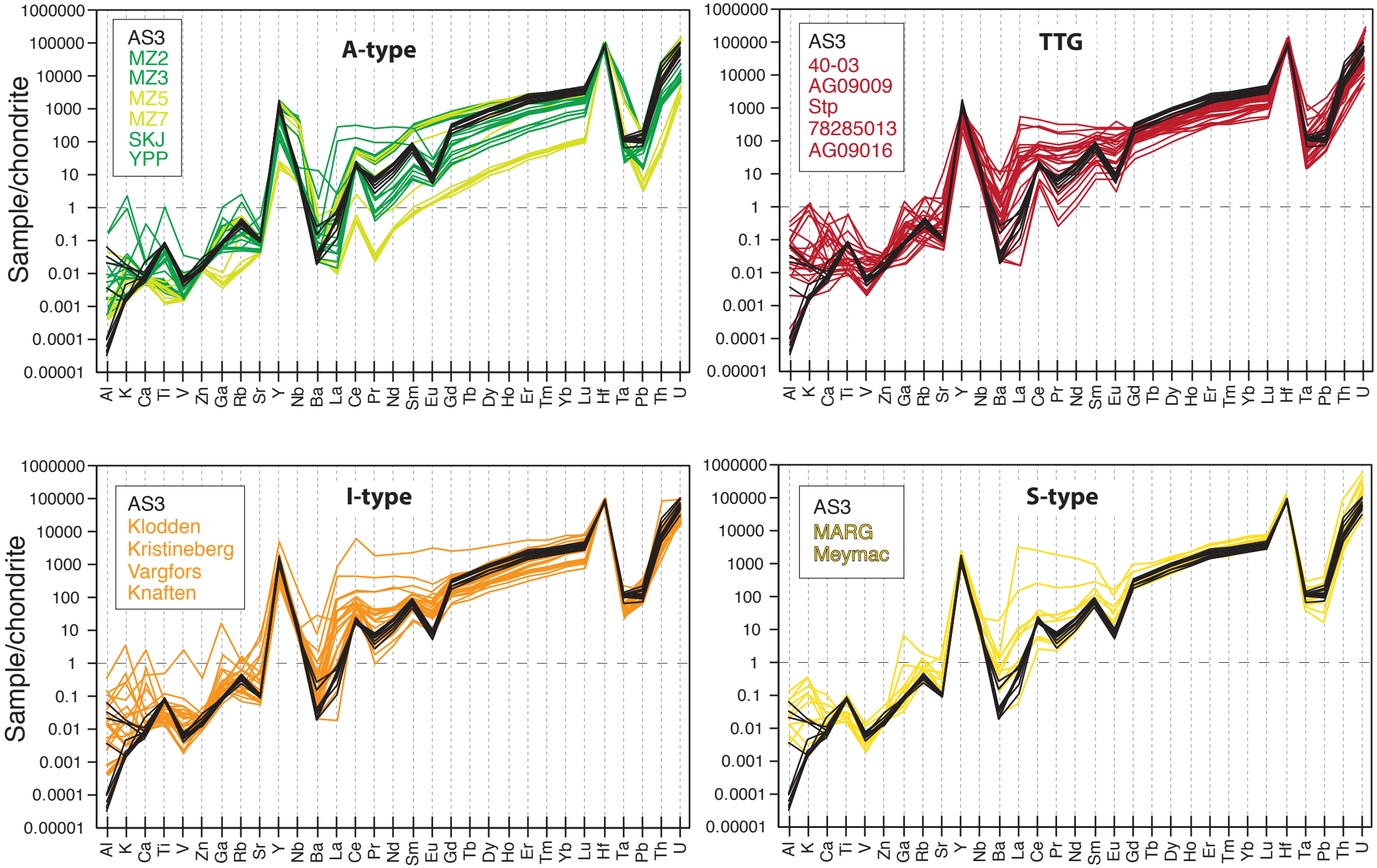
A-type
AS3
MZ2
MZ3
MZ5
MZ7
SKJ
YPP
TTG
AS3
40-03
AG09009
Stp
78285013
AG09016
I-type
AS3
Klodden
Kristineberg
Vargfors
Knaften
S-type
AS3
MARG
Meymac
Sample/chondrite
1000000
100000
10000
1000
100
10
1
0.1
0.01
0.001
0.0001
0.00001
Al K Ca Ti V Zn Ga Rb Sr Y Nb Ba La Ce Pr Nd Sm Eu Gd Tb Dy Ho Er Tm Yb Lu Hf Ta Pb Th U

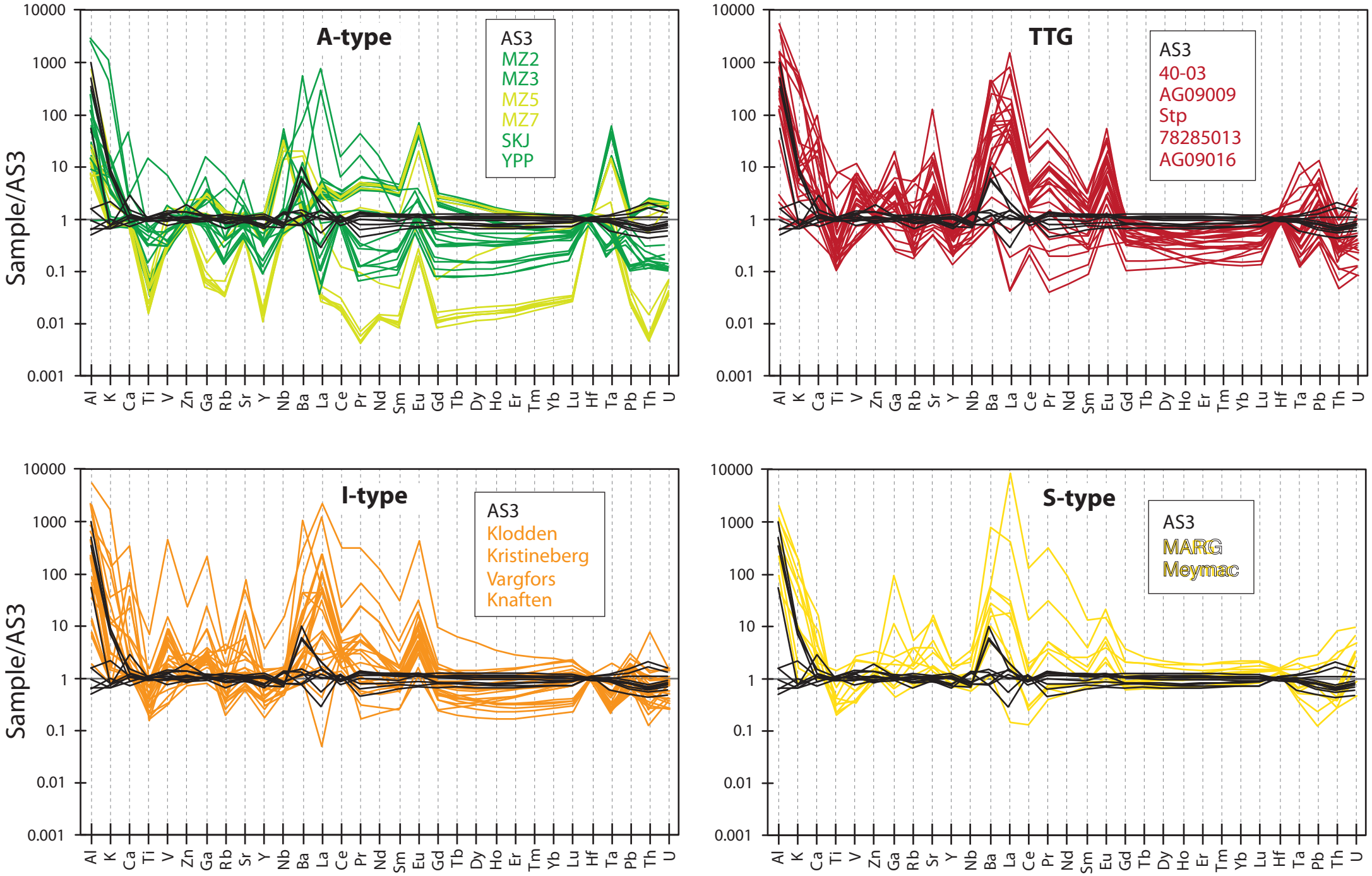
A-type
AS3
MZ2
MZ3
MZ5
MZ7
SKJ
YPP
TTG
AS3
40-03
AG09009
Stp
78285013
AG09016
I-type
AS3
Klodden
Kristineberg
Vargfors
Knaften
S-type
AS3
MARG
Meymac
Sample/AS3
10000
1000
100
10
1
0.1
0.01
0.001
Al K Ca Ti V Zn Ga Rb Sr Y Nb Ba La Ce Pr Nd Sm Eu Gd Tb Dy Ho Er Tm Yb Lu Hf Ta Pb Th U

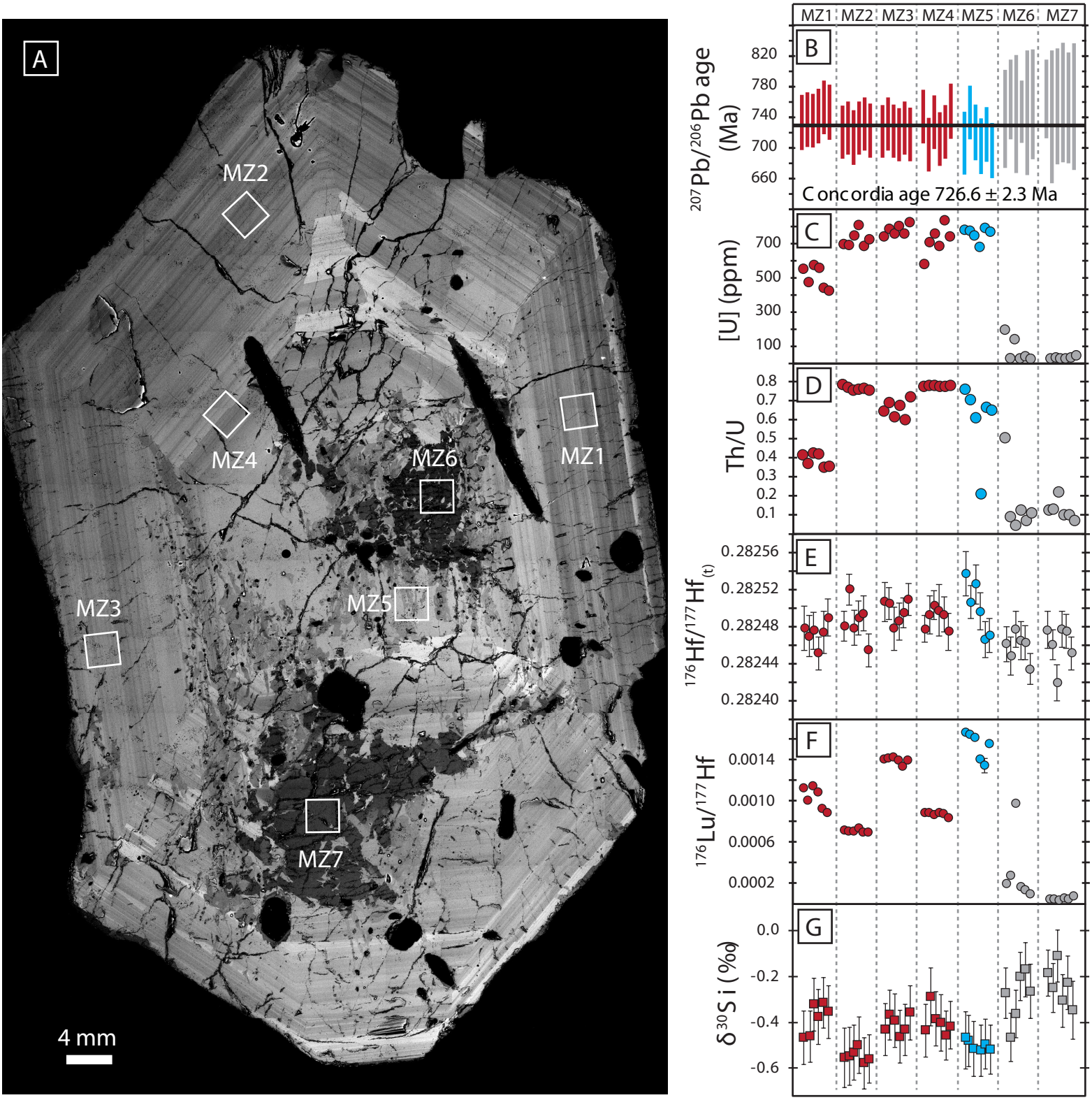
A
MZ2
MZ4
MZ6
MZ1
MZ3
MZ5
MZ7
4 mm
MZ1 MZ2 MZ3 MZ4 MZ5 MZ6 MZ7
B
$^{207}Pb/^{206}Pb$ age (Ma)
820
780
740
700
660
Concordia age 726.6 ± 2.3 Ma
C
[U] (ppm)
700
500
300
100
D
Th/U
0.8
0.7
0.6
0.5
0.4
0.3
0.2
0.1
E
$^{176}Hf/^{177}Hf_{(t)}$
0.28256
0.28252
0.28248
0.28244
0.28240
F
$^{176}Lu/^{177}Hf$
0.0014
0.0010
0.0006
0.0002
G
$\delta^{30}Si$ (‰)
0.0
-0.2
-0.4
-0.6

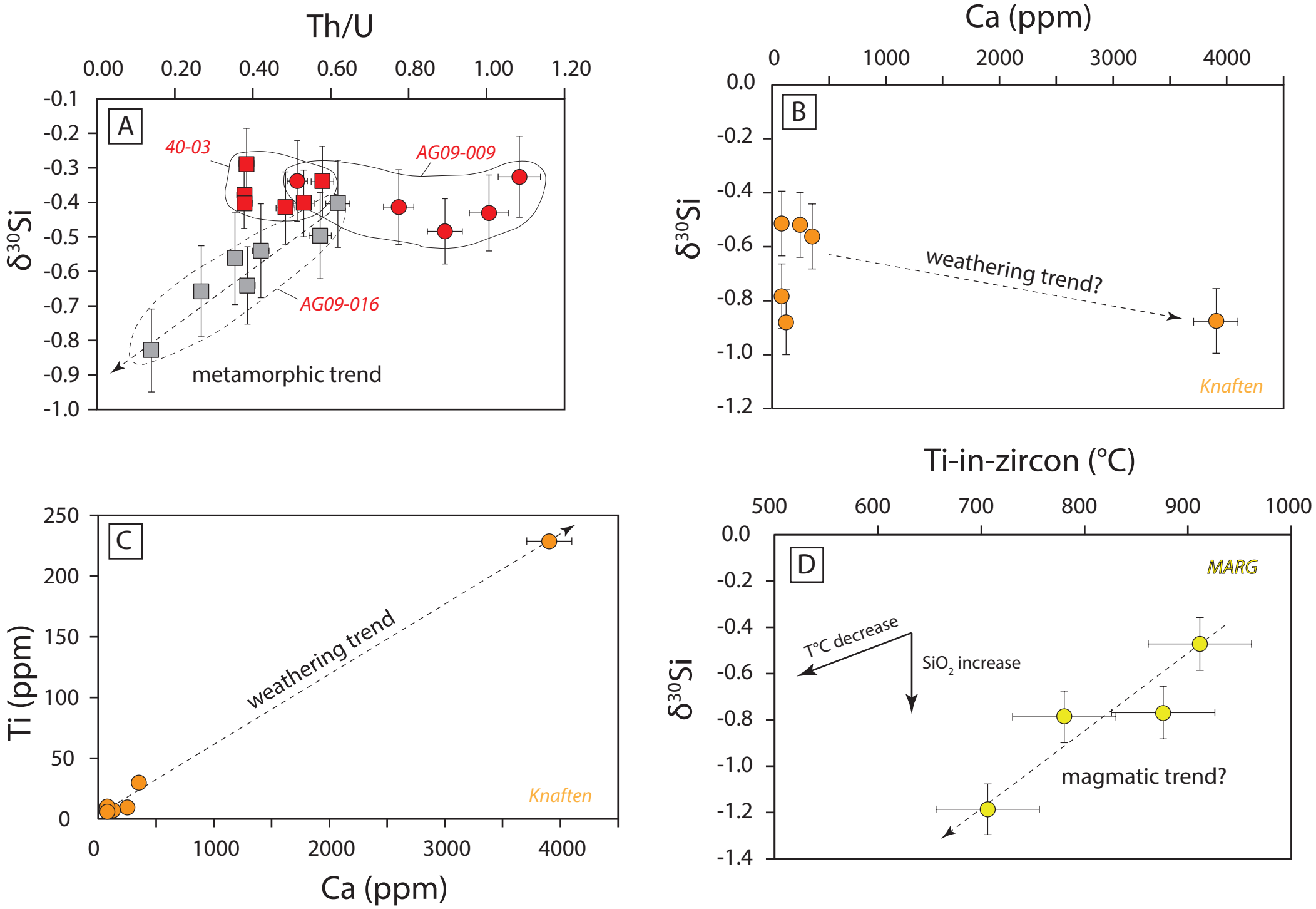
Th/U
0.00
0.20
0.40
0.60
0.80
1.00
1.20
A
40-03
AG09-009
AG09-016
metamorphic trend
δ30Si
-0.1
-0.2
-0.3
-0.4
-0.5
-0.6
-0.7
-0.8
-0.9
-1.0
Ca (ppm)
0
1000
2000
3000
4000
B
weathering trend?
Knaften
0.0
-0.2
-0.4
-0.6
-0.8
-1.0
-1.2
C
weathering trend
Knaften
Ti (ppm)
250
200
150
100
50
0
Ca (ppm)
Ti-in-zircon (°C)
500
600
700
800
900
1000
D
MARG
T°C decrease
SiO2 increase
magmatic trend?
-1.4

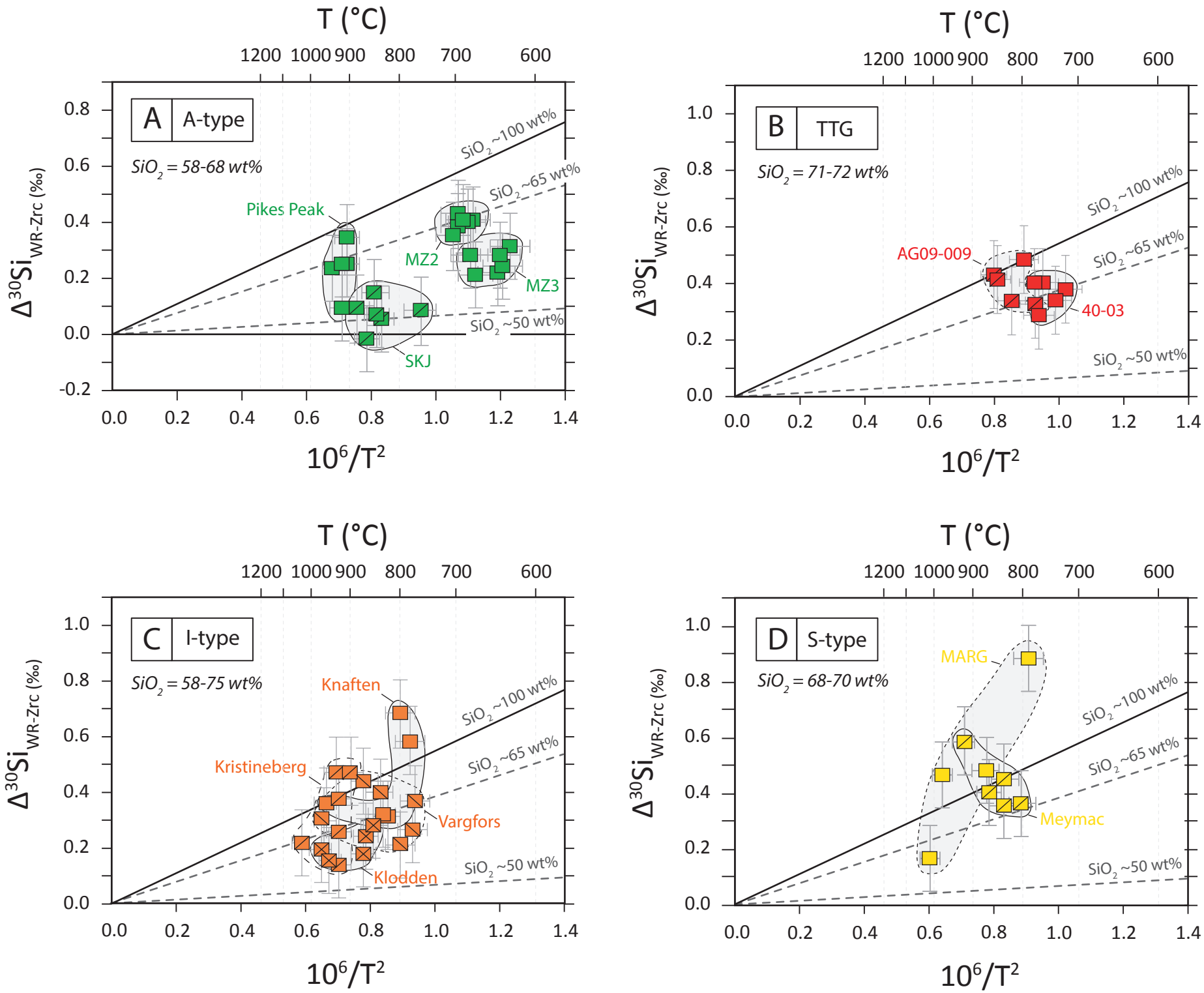
T (°C)
1200 1000 900 800 700 600
A A-type
SiO2 = 58-68 wt%
SiO2 ~100 wt%
SiO2 ~65 wt%
SiO2 ~50 wt%
Pikes Peak
MZ2
MZ3
SKJ
Δ30SiWR-Zrc (‰)
10⁶/T²
B TTG
SiO2 = 71-72 wt%
AG09-009
40-03
C I-type
SiO2 = 58-75 wt%
Knaften
Kristineberg
Vargfors
Klodden
D S-type
SiO2 = 68-70 wt%
MARG
Meymac

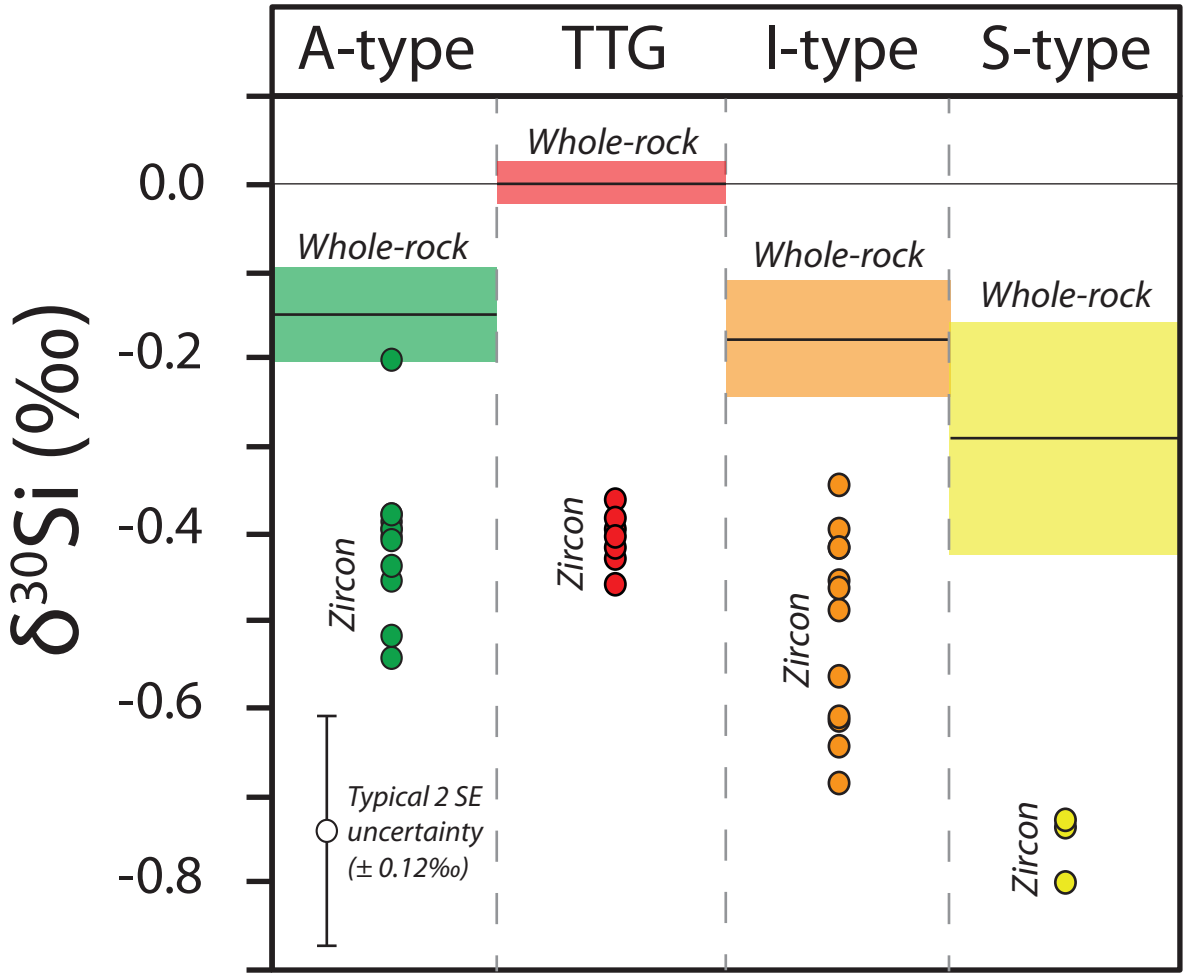
A-type
TTG
I-type
S-type
Whole-rock
Whole-rock
Whole-rock
Whole-rock
Zircon
Zircon
Zircon
Zircon
Typical 2 SE uncertainty (± 0.12‰)
0.0
-0.2
-0.4
-0.6
-0.8
δ30Si (‰)

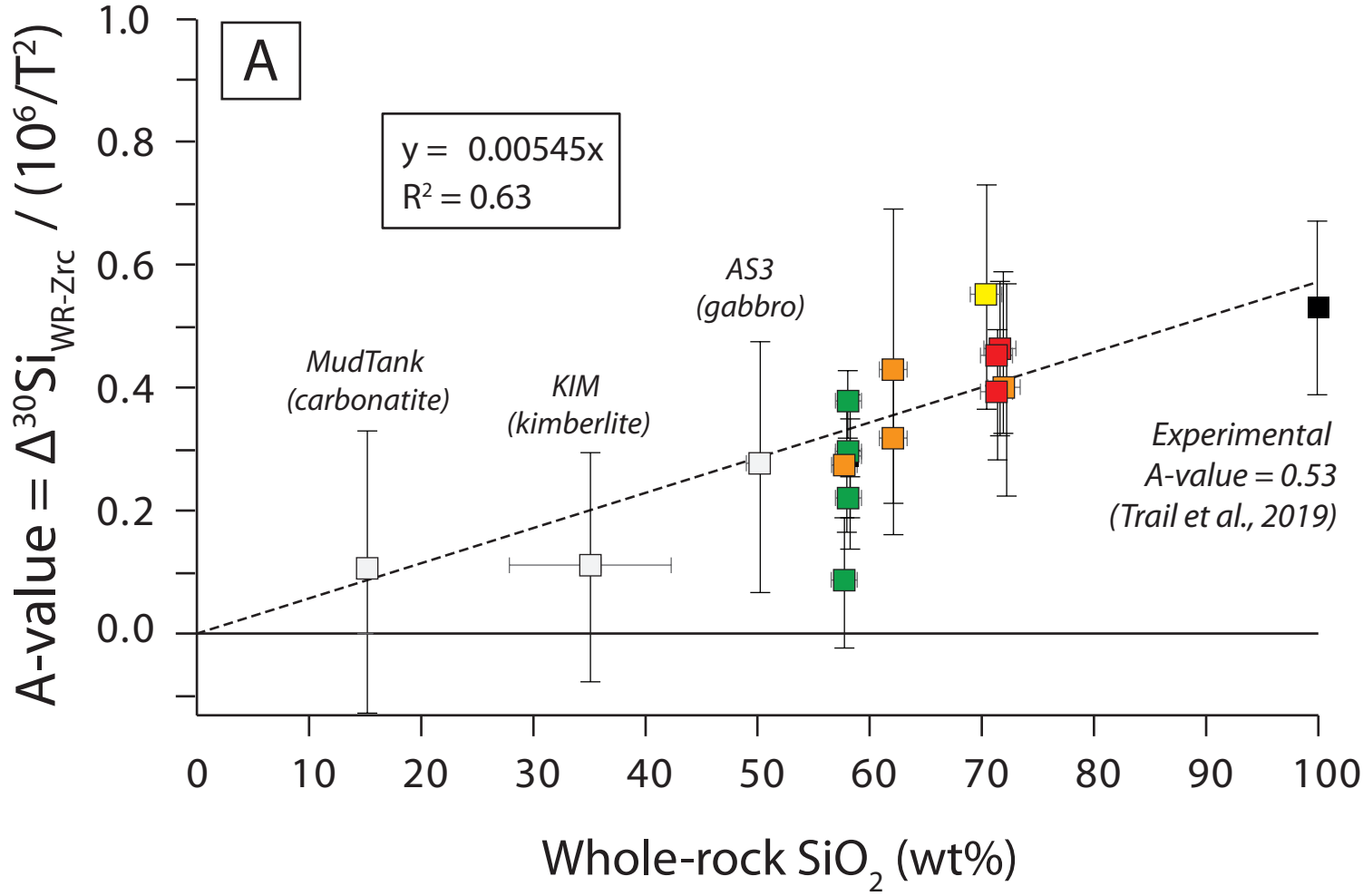
A
y = 0.00545x
R² = 0.63
MudTank
(carbonatite)
KIM
(kimberlite)
AS3
(gabbro)
Experimental
A-value = 0.53
(Trail et al., 2019)
A-value = Δ30SiWR-Zrc / (10⁶/T²)
Whole-rock SiO2 (wt%)
1.0
0.8
0.6
0.4
0.2
0.0
0
10
20
30
40
50
60
70
80
90
100

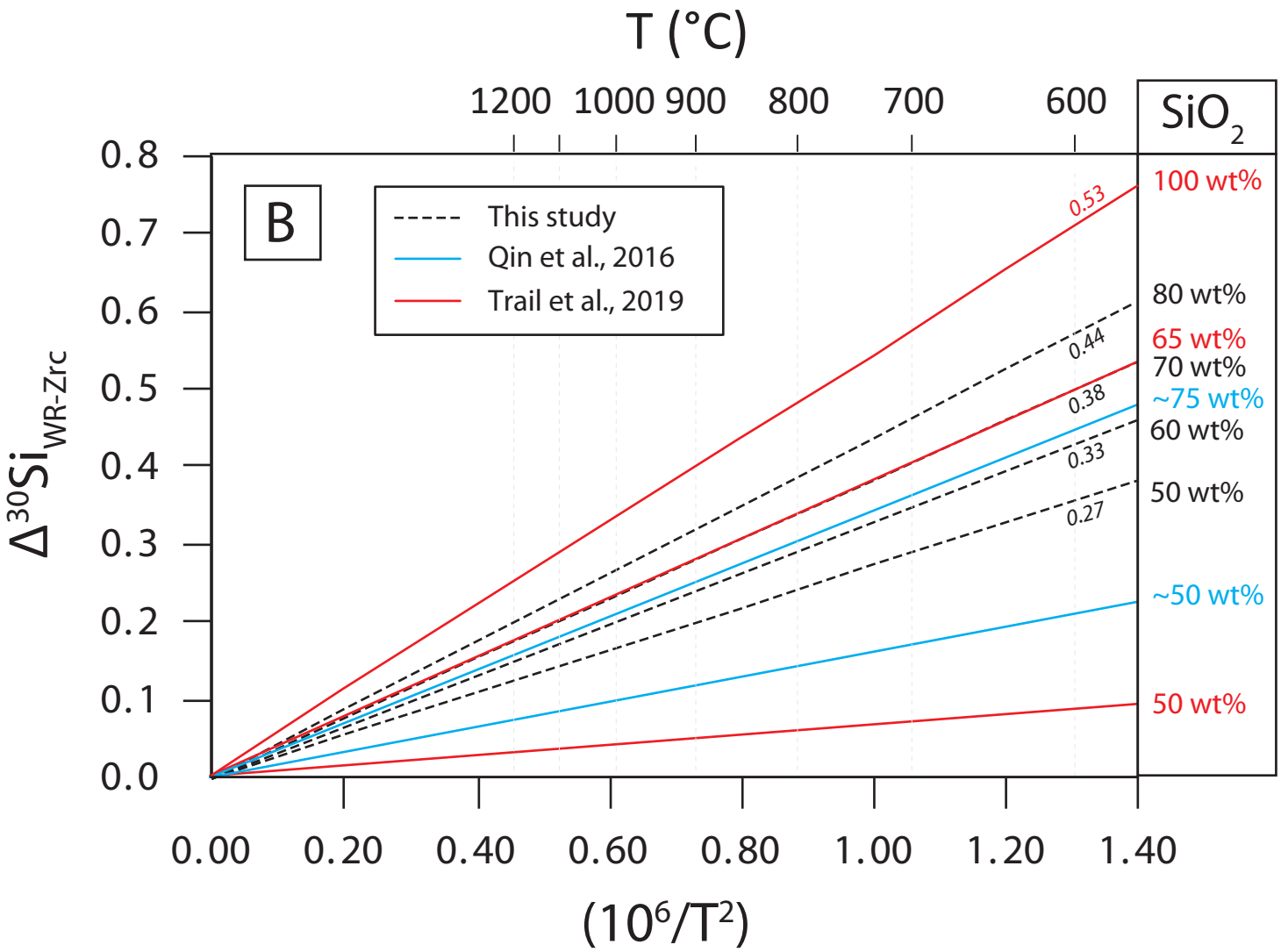
T (°C)
1200
1000
900
800
700
600
SiO2
B
This study
Qin et al., 2016
Trail et al., 2019
0.53
0.44
0.38
0.33
0.27
100 wt%
80 wt%
65 wt%
70 wt%
~75 wt%
60 wt%
50 wt%
~50 wt%
50 wt%
Δ30SiWR-Zrc
0.8
0.7
0.6
0.5
0.4
0.3
0.2
0.1
0.0
0.00
0.20
0.40
0.60
0.80
1.00
1.20
1.40
(10⁶/T²)

Stable isotope geochemistry of silicon in granitic zircon

Highlights :

- Zircons from various granite types were analyzed for Si isotopes
- Si isotopes were measured using laser-ablation and solution MC-ICP-MS
- Metamorphism and alteration can modify zircon Si isotope composition
- Si isotope fractionation in zircon is controlled by temperature and melt SiO_2 wt%
- Si isotopes in zircon can discriminate granite types and track magma evolution

Declaration of interests

☒ The authors declare that they have no known competing financial interests or personal relationships that could have appeared to influence the work reported in this paper.

☐The authors declare the following financial interests/personal relationships which may be considered as potential competing interests: